

## ACCRETION RATE AND THE PHYSICAL NATURE OF UNOBSCURED ACTIVE GALAXIES<sup>1</sup>

JONATHAN R. TRUMP,<sup>2</sup> CHRISTOPHER D. IMPEY,<sup>2</sup> BRANDON C. KELLY,<sup>3,4</sup> FRANCESCA CIVANO,<sup>3</sup> JARED M. GABOR,<sup>2</sup>  
ALEKSANDAR M. DIAMOND-STANIC,<sup>2</sup> ANDREA MERLONI,<sup>5</sup> C. MEGAN URRY,<sup>6</sup> HENG HAO,<sup>3</sup> KNUD JAHNKE,<sup>7</sup> TOHRU  
NAGAO,<sup>8</sup> YOSHI TANIGUCHI,<sup>8</sup> ANTON M. KOEKEMOER,<sup>9</sup> GIORGIO LANZUISI,<sup>3</sup> CHARLES LIU,<sup>10,11</sup> VINCENZO MAINIERI,<sup>12</sup>  
MARA SALVATO,<sup>5</sup> AND NICK Z. SCOVILLE<sup>13</sup>

*Draft version October 29, 2018*

### ABSTRACT

We show how accretion rate governs the physical properties of a sample of unobscured broad-line, narrow-line, and lineless active galactic nuclei (AGNs). We avoid the systematic errors plaguing previous studies of AGN accretion rate by using accurate accretion luminosities ( $L_{int}$ ) from well-sampled multiwavelength SEDs from the Cosmic Evolution Survey (COSMOS), and accurate black hole masses derived from virial scaling relations (for broad-line AGNs) or host-AGN relations (for narrow-line and lineless AGNs). In general, broad emission lines are present only at the highest accretion rates ( $L_{int}/L_{Edd} > 10^{-2}$ ), and these rapidly accreting AGNs are observed as broad-line AGNs or possibly as obscured narrow-line AGNs. Narrow-line and lineless AGNs at lower specific accretion rates ( $L_{int}/L_{Edd} < 10^{-2}$ ) are unobscured and yet lack a broad line region. The disappearance of the broad emission lines is caused by an expanding radiatively inefficient accretion flow (RIAF) at the inner radius of the accretion disk. The presence of the RIAF also drives  $L_{int}/L_{Edd} < 10^{-2}$  narrow-line and lineless AGNs to 10 times higher ratios of radio to optical/UV emission than  $L_{int}/L_{Edd} > 10^{-2}$  broad-line AGNs, since the unbound nature of the RIAF means it is easier to form a radio outflow. The IR torus signature also tends to become weaker or disappear from  $L_{int}/L_{Edd} < 10^{-2}$  AGNs, although there may be additional mid-IR synchrotron emission associated with the RIAF. Together these results suggest that specific accretion rate is an important physical “axis” of AGN unification, described by a simple model.

*Subject headings:* galaxies: active — galaxies: nuclei — quasars: emission lines — accretion, accretion disks

### 1. INTRODUCTION

<sup>1</sup> Based on observations with the XMM-Newton Observatory, an ESA science mission with instruments and contributions directly funded by ESA Member States and NASA; the Magellan Telescope, operated by the Carnegie Observatories; the European Southern Observatory (ESO) Very Large Telescope (VLT); and the MMT Observatory, a joint facility of the University of Arizona and the Smithsonian Institution; the Subaru Telescope, operated by the National Astronomical Observatory of Japan; and the NASA/ESA *Hubble Space Telescope*, operated at the Space Telescope Science Institute, which is operated by AURA Inc, under NASA contract NAS 5-26555.

<sup>2</sup> Steward Observatory, University of Arizona, 933 North Cherry Avenue, Tucson, AZ 85721 USA

<sup>3</sup> Harvard-Smithsonian Center for Astrophysics, 60 Garden Street, Cambridge, MA 02138 USA

<sup>4</sup> Hubble Fellow

<sup>5</sup> Max Planck-Institut für Extraterrestrische Physik, Giessenbachstrasse 1, D-85748 Garching, Germany

<sup>6</sup> Physics Department and Yale Center for Astronomy and Astrophysics, Yale University, New Haven, CT 06511, USA

<sup>7</sup> Max Planck Institut für Astronomie, Königstuhl 17, D-69117 Heidelberg, Germany

<sup>8</sup> Research Center for Space and Cosmic Evolution, Ehime University, 2-5 Bunkyo-cho, Matsuyama 790-8577, Japan

<sup>9</sup> Space Telescope Science Institute, 3700 San Martin Drive, Baltimore, MD 21218 USA

<sup>10</sup> Astrophysical Observatory, Department of Engineering Science and Physics, City University of New York, College of Staten Island, 2800 Victory Blvd., Staten Island, NY 10314

<sup>11</sup> Hayden Planetarium, American Museum of Natural History, Central Park West at 79th Street, New York, NY 10024 USA

<sup>12</sup> European Southern Observatory, Karl-Schwarzschild-Strasse 2, D-85748 Garching, Germany

<sup>13</sup> California Institute of Technology, MC 105-24, 1200 East California Boulevard, Pasadena, CA 91125 USA

Supermassive black holes (SMBHs) are now known to be ubiquitous in the centers of all massive galaxies (Magorrian et al. 1998). SMBHs grow in an “active” phase of accretion, during which they are observed as active galactic nuclei (AGN). AGN growth is intimately tied to galaxy evolution, as evident in the well-studied correlations between SMBH mass ( $M_{BH}$ ) and properties of the host galaxy bulge (e.g., Gebhardt et al. 2000; Ferrarese & Merritt 2000; Marconi & Hunt 2003). The AGN phase is also hypothesized to regulate star formation in its host galaxy, with the galaxy feeding the black hole in turn (e.g. Di Matteo, Springel, & Hernquist 2005; Younger et al. 2008). All massive galaxies are thought to experience episodic AGN behavior in their lifetime (Soltan 1982; Marconi et al. 2004).

AGNs are generally classified by differences in their optical spectra. Type 1 or broad-line AGNs have broad ( $v_{FWHM} \gtrsim 1000 \text{ km s}^{-1}$ ) emission lines superimposed on blue unobscured continua in the UV/optical (e.g., Vanden Berk et al. 2001), and are the most luminous persistent sources in the sky. Type 2 or narrow-line AGNs lack broad emission lines and have weaker continua (frequently dominated by their host galaxies), but have strong narrow emission lines, especially from forbidden transitions. Narrow emission lines associated with nuclear activity can be distinguished from lines caused by star formation by studying the line ratios (Baldwin, Phillips, & Terlevich 1981). The line ratio diagnostics work because the “harder” emission of an AGN is more efficient at ionizing the surrounding gas and dust than star formation, and thus AGNs have

stronger lines from high-energy forbidden transitions (e.g., [OIII]  $\lambda 5007\text{\AA}$  and [NII]  $\lambda 6583\text{\AA}$ ) relative to the lower-energy hydrogen transitions (e.g., H $\beta$   $\lambda 4861\text{\AA}$  and H $\alpha$   $\lambda 6563\text{\AA}$ ). The subclass of “low-ionization nuclear emission region” AGNs (LINERs, Heckman 1980) have narrow emission lines that are probably excited by some combination of ionization from both star formation and an AGN (Eracleous et al. 2010). Deep X-ray surveys have additionally revealed “optically dull” AGNs (Elvis et al. 1981; Comastri et al. 2002), which have bright X-ray emission but none of the broad or narrow emission line signatures of AGN accretion. While many optically dull AGNs can be explained as Type 2 AGNs diluted by prominent host galaxies (Moran, Filippenko & Chornock 2002; Caccianiga et al. 2007), at least  $\sim 1/3$  are undiluted but intrinsically optically weaker than other AGNs (Trump et al. 2009c). The inferred X-ray column density  $N_H$  can also be used to classify AGNs, with Type 2 (narrow-line) AGNs typically more X-ray absorbed than Type 1 (broad-line) AGNs. However X-ray and optical classifications differ for  $\sim 20\%$  of objects (Trouille et al. 2009).

Historically, Type 2 and optically dull AGNs have been described as obscured versions of Type 1 AGN, with the broad emission line region (BLR) hidden behind a partially opaque “torus” of gas and dust, while the narrow emission lines lie outside the torus (e.g., Krolik & Begelman 1988). The best evidence for this scenario is the observation that some Type 2 AGNs have a “hidden” BLR revealed by spectropolarimetry (Antonucci 1993). However, recent observations have revealed several serious limitations of a simple unified model based solely on geometric obscuration. Even in very deep spectropolarimetric observations, many Type 2 AGNs show no hidden BLR (Barth, Filippenko & Moran 1999; Tran 2001; Wang & Zhang 2007). Observations suggest a lower  $L/L_{Edd} \geq 0.01$  limit in accretion rate for broad-line AGNs (Kollmeier et al. 2006; Trump et al. 2009b), although they remain incomplete at low accretion rates and low masses (Kelly et al. 2010). The X-ray spectra are unabsorbed ( $N_H \lesssim 10^{21} \text{ cm}^{-2}$ ) for 30-40% of Type 2 AGNs (Mainieri et al. 2007; Trouille et al. 2009), as well as most local LINERs (Ho 2008, and references therein) and distant optically dull AGNs (Trump et al. 2009c). Several well-studied LINERs additionally lack the narrow Fe K $\alpha$  emission signature of a dusty torus (Ptak et al. 2004; Bianchi et al. 2008). Many Type 2 AGNs and most optically dull AGNs have mid-IR colors like normal galaxies (Ho 2008; Trump et al. 2009c), in contrast to hot mid-IR colors of Type 1 AGNs described by torus models (Nenkova et al. 2008; Mor, Netzer, & Elitzur 2009). Toroidal obscuration is additionally ruled out for some strongly varying Type 2 (Hawkins 2004) and optically dull AGNs (Trump et al. 2009c), since these objects have continua which vary on year timescales, well within the inferred light travel time dimension of any torus.

Several authors have proposed models which use different accretion rates as a cause of the differences between observed AGNs. Elitzur & Ho (2009) suggest that the BLR and “torus” are inner (ionized) and outer (clumpy and dusty) parts of the same disk-driven wind, and that this wind is no longer supported at low accretion rate

(see also Elitzur & Shlosman 2006; Nenkova et al. 2008). Similarly, Nicastro (2000) suggested that low accretion rates actually drive the disk wind within the last stable orbit of the SMBH, meaning that the BLR cannot form. Models for radiatively inefficient accretion (e.g., Yuan 2007) suggest that at  $L/L_{Edd} \lesssim 10^{-2}$ , the accretion disk becomes truncated near the SMBH, with a geometrically thick and optically thin disk at low radii, and a normal thin disk (e.g., Shakura & Sunyaev 1973) at higher radii. Such objects are predicted to lack strong emission lines (both broad and narrow) and have weak UV/optical emission, as observed in many optically weak low-luminosity AGNs (Ho 2009) and X-ray bright, optically dull AGNs (Trump et al. 2009c). Hopkins et al. (2009) additionally show that X-ray hardness, generally attributed to X-ray absorption, may also result from the naturally X-ray hard spectrum expected from radiatively inefficient accretion.

In this work we directly measure Eddington ratios for a large, X-ray selected sample of broad-line, narrow-line, and lineless AGNs. The Eddington ratio is a unitless measure of accretion power, defined as  $\lambda \equiv L_{int}/L_{Edd}$ . (with  $L_{int}$  the intrinsic accretion luminosity). The sample is drawn from the Cosmic Evolution Survey (COSMOS, Scoville et al. 2007) X-ray AGN sample (Trump et al. 2007), as described in Section 2. Estimates of specific accretion rates are described in Section 3, with intrinsic accretion luminosity  $L_{int}$  measured directly from fits to the multiwavelength continuum (avoiding uncertain bolometric corrections) and black hole masses from the broad line scaling relations (for broad-line AGNs) or the  $M_{BH} - M_*$  relations (for narrow-line and lineless AGNs). In Section 4 we show that broad emission lines are present at only high accretion rates ( $L_{int}/L_{Edd} > 0.01$ ), while narrow-line and lineless AGNs at lower accretion rates have cooler disks, stronger radio jets, and no torus IR signature. We present a “cartoon” model which summarizes our results in Section 5, with predictions for future observations in Section 6. We adopt a cosmology with  $h = 0.70$ ,  $\Omega_M = 0.3$ ,  $\Omega_\Lambda = 0.7$  throughout.

## 2. OBSERVATIONAL DATA

Measuring an accurate specific accretion rate requires accurate accretion luminosities and black hole mass estimates. In particular, SED measurements from optical/UV to X-ray are necessary to constrain intrinsic luminosities to within a factor of a few (as we show in §3.1). We select a sample of 348 AGNs from the Cosmic Evolution Survey (COSMOS, Scoville et al. 2007) field, which is based on the 1.7 deg<sup>2</sup> HST/ACS mosaic (Koekemoer et al. 2007). These AGNs have multiwavelength data in the form of Spitzer/IRAC, HST/ACS, Subaru/Suprime-Cam, GALEX, XMM-Newton, and Chandra observations, as described in Table 1. Spectroscopic identification and redshifts for these objects comes from archival SDSS data, Magellan/IMACS and MMT/Hectospec (Trump et al. 2009a), and VLT/VIMOS observations (Lilly et al. 2007).

The sample is selected from the parent catalog of 1651 XMM-COSMOS point sources with optical counterparts (Brusa et al. 2010), limited by  $f_{0.5-2\text{keV}} > 2 \times 10^{-16} \text{ erg s}^{-1} \text{ cm}^{-2}$ . Of these X-ray point sources, 649 objects

with  $i_{AB} < 23.5$  have high-confidence ( $> 90\%$  likelihood as correct) identifications and redshifts from optical spectroscopy (Trump et al. 2009a; Lilly et al. 2007) in COSMOS. Most of the X-ray point sources without spectroscopy were missed simply due to random slit placement constraints. The optical spectroscopy is  $\sim 90\%$  complete to  $i_{AB} < 22.5$ , although the completeness is redshift-dependent. For broad-line AGNs, the spectroscopic completeness is lower at  $0.5 < z < 1$ ,  $z \sim 1.4$ , and  $z \sim 2.4$ , especially at  $i_{AB} > 22.5$  (see Figure 13 of Trump et al. 2009a). For narrow-line and lineless AGNs, spectroscopic completeness drops dramatically at  $z > 1.2$ , since at higher redshifts the  $4000\text{\AA}$  break and the [OII] feature shift redward of the observed wavelength range. To ensure that X-ray objects with narrow-line and lineless spectra are bona-fide AGNs, we select only objects with  $L_{0.5-10\text{keV}} > 3 \times 10^{42} \text{ erg s}^{-1}$ . This X-ray luminosity limit is generally used to separate AGNs from X-ray fainter starburst galaxies (e.g., Hornschemeier et al. 2001). We also include seven broad-line AGNs without X-ray detection, six of which were selected by their Spitzer/IRAC colors and one which is a serendipitous object from the bright zCOSMOS survey (which selected targets based only on  $i_{AB} < 22.5$ ). While these 7 X-ray undetected AGNs do not come from a complete sample, we include them to gain a larger parameter space of AGN spectral types and accretion rates (in effect, when using their X-ray limits, they occupy the same  $L_{disk}/L_X$  parameter space as a few other X-ray detected AGNs). Restricting narrow-line and lineless AGNs to be X-ray luminous and adding the 7 X-ray undetected broad-line AGNs makes a parent sample of 380 broad-line, 124 narrow-line, and 49 lineless AGNs (553 total) with high-confidence redshifts and spectral identification.

Measuring accurate black hole masses additionally constrains the sample to certain redshift ranges. For Type 1 AGNs, we require the presence of one of the CIV, MgII, or H $\beta$  broad emission lines in the observed spectral range, effectively limiting broad-line AGNs with IMACS or VIMOS spectra to  $0.16 < z < 0.88$ ,  $1 < z < 2.4$ , and  $2.7 < z < 4.9$  and objects with Hectospec or SDSS spectra to  $z < 4.9$ . For narrow-line and lineless AGNs, we estimate black hole mass from the  $M_{BH} \sim L_{bulge}$  relation, and so we require an accurate estimate of  $L_{bulge}$ . For this we use the sample of objects in COSMOS with morphological decompositions (Gabor et al. 2009) from the HST/ACS images (Koekemoer et al. 2007), which also effectively limits the narrow-line and lineless AGNs to  $z < 1.2$  (beyond which the  $4000\text{\AA}$  break shifts out of the ACS- $i$  band and the host galaxy is much more difficult to detect). The accurate host measurements from Gabor et al. (2009) additionally allow us to subtract the host component before computing the intrinsic bolometric luminosity. In general, the narrow-line and lineless AGNs are biased towards lower redshift and consequently higher mass, since AGNs grow over the cosmic time. The narrow-line and lineless AGNs have a mean redshift of 0.7, while the broad-line AGNs have a mean redshift of 1.6. The final sample of 348 AGNs includes 256 broad-line, 65 narrow-line, and 27 lineless AGNs.

Full multiwavelength data exist for  $> 95\%$  of the AGNs in the sample in every wavelength region except the UV. X-ray data exist from both Chandra and XMM-

Newton: we use the deeper Chandra data when available, but the Chandra observations cover only the central  $0.8 \text{ deg}^2$  of the COSMOS field. For the 7 X-ray undetected broad-line AGNs, we use the 0.5-2 keV XMM flux limit ( $f_{0.5-2\text{keV}} = 2 \times 10^{-16} \text{ erg s}^{-1} \text{ cm}^{-2}$ ) for their X-ray luminosity (since these AGNs have  $L_{disk}/L_X > 10$ , their bolometric luminosity is dominated by their optical/UV emission and completely neglecting their X-ray emission does not significantly change their bolometric luminosity estimate). We apply the zero-point offsets derived by Ilbert et al. (2009) to the IR-UV photometry.

## 2.1. Measuring Absorption and Extinction

X-ray absorption and optical/UV extinction could pose a challenge to measuring the intrinsic accretion power. The most heavily absorbed AGNs (e.g. Compton-thick AGNs with  $N_H > 10^{24} \text{ cm}^{-2}$ ) are entirely missed by our survey because they lack detectable X-ray emission (e.g., Treister et al. 2004). But if an AGN is moderately absorbed and still X-ray detected, we might expect its disk to appear cooler because the UV light is preferentially extinguished, and its X-ray slope to appear harder because the soft X-rays are preferentially absorbed. Some AGNs are also intrinsically reddened, decreasing their UV emission by a factor of 2-3 (Richards et al. 2003) and causing us to underestimate their accretion disk emission. With absorbed soft X-rays and extinguished disk emission, we could significantly underestimate  $L_{int}/L_{Edd}$ .

We use X-ray column density  $N_H$  to characterize the obscuration properties of our AGNs. Column density and optical extinction are roughly correlated, with  $A_V/N_H \sim 2 \times 10^{-23} \text{ cm}^2$  (Martinez-Sansigre et al. 2006). Then at  $N_H < 10^{22} \text{ cm}^{-2}$ , optical magnitude should be extinguished by  $\lesssim 20\%$  ( $\lesssim 0.2 \text{ mag}$ ). Assuming a SMC reddening law (Pei 1992), as is most appropriate for AGNs, this optical extinction translates to a factor of  $\sim 1.2$  extinction at  $3000\text{\AA}$  in the UV. Maiolino et al. (2001) showed that the  $A_V - N_H$  relation varies by up to a factor of 30 because of unknown changes in the gas-to-dust ratio, grain size, and/or different physical locations of the optical and X-ray absorbing material. However for all AGNs in the Maiolino et al. (2001) sample with  $L_X > 10^{42} \text{ erg s}^{-1}$ ,  $A_V/N_H < 1.8 \times 10^{-22} \text{ cm}^2$ , meaning at  $N_H \sim 10^{22} \text{ cm}^{-2}$  even the maximum optical (V-band) extinction is a factor of 5 and the maximum UV ( $3000\text{\AA}$ ) extinction a factor of 30.

Column density  $N_H$  can be accurately measured for the 153 AGNs (93 broad-line, 38 narrow-line, 22 lineless AGNs) in the sample which have  $> 40$  XMM or Chandra counts. (With less than 40 counts, the spectral fitting does not always stably converge.) We fit each X-ray spectrum as an intrinsically absorbed power-law with Galactic absorption ( $N_{H,\text{gal}} = 2.6 \times 10^{20} \text{ cm}^2$  in the direction of the COSMOS field), with the power-law slope and  $N_H$  as free parameters. The best-fit  $N_H$  value and its error are found using the Cash (1979) statistic. We present  $N_H$  and X-ray slope  $\Gamma$  in Figure 1. Among the 153 AGNs with  $> 40$  X-ray counts, there are 118 unobscured AGNs with  $N_H < 10^{22} \text{ cm}^{-2}$  (82 broad-line, 24 narrow-line, and 12 lineless AGNs). We restrict our main conclusions to this set of 118 unobscured AGNs for the remainder of this work.

TABLE 1  
 COSMOS MULTIWAVELENGTH DATA

Band	Telescope	Wavelength Å	Energy eV	Limit AB mag <sup>b</sup>	NL/LL AGNs Detected	BL AGNs Detected	Reference <sup>a</sup>
$X_{hard}$	Chandra	1.24-6.20	2000-10000	$7.3 \times 10^{-16}$	79/92	228/256	(1)
$X_{hard}$	XMM	1.24-6.20	2000-10000	$9.3 \times 10^{-15}$	79/92	228/256	(2)
$X_{soft}$	Chandra	6.20-24.8	500-2000	$1.9 \times 10^{-16}$	88/92	249/256	(1)
$X_{soft}$	XMM	6.20-24.8	500-2000	$1.7 \times 10^{-15}$	88/92	249/256	(2)
FUV	GALEX	1426-1667	7.44-8.63	25.7	27/92	131/256	(3)
NUV	GALEX	1912-2701	4.59-6.84	26.0	55/92	184/256	(3)
u*	CFHT	3642-4180	2.97-3.40	26.4	92/92	254/256	(4)
$B_J$	Subaru	4036-4843	2.56-3.07	27.7	92/92	256/256	(4)
$g^+$	Subaru	4347-5310	2.33-2.85	27.1	92/92	256/256	(4)
$V_J$	Subaru	4982-5916	2.10-2.49	27.0	92/92	255/256	(4)
$r^+$	Subaru	5557-6906	1.80-2.23	27.1	92/92	256/256	(4)
i*	CFHT	6140-9119	1.36-2.02	26.7	92/92	256/256	(4)
F814W	HST/ACS	7010-8880	1.40-1.77	27.2	92/92	256/256	(5)
$z^+$	Subaru	8544-9499	1.31-1.45	25.7	92/92	254/256	(4)
J	UKIRT	11665-13223	0.94-1.06	23.8	92/92	256/256	(4)
Ks	CFHT	19900-23050	0.538-0.623	23.4	92/92	253/256	(6)
IRAC1	Spitzer	31557-38969	0.318-0.383	23.9	91/92	255/256	(4)
IRAC2	Spitzer	39550-49663	0.250-0.313	23.3	91/92	255/256	(4)
IRAC3	Spitzer	50015-63514	0.195-0.248	21.3	91/92	255/256	(4)
IRAC4	Spitzer	62832-91229	0.136-0.197	21.0	91/92	255/256	(4)
1.4 GHz	VLA	$2 \times 10^9$	$6 \times 10^{-6}$	$20 \mu\text{Jy}$	92/92	256/256	(7)

<sup>a</sup> References are as follows: (1) Elvis et al. (2009), (2) Cappelluti et al. (2009), (3) Zamojski et al. (2007), (4) Capak et al. (2010), (5) Koekemoer et al. (2007), (6) McCracken et al. (2010), (7) Schinnerer et al. (2007)

<sup>b</sup> X-ray flux limits are given in  $\text{erg s}^{-1} \text{cm}^{-2}$ , and the radio flux limit is given in  $\mu\text{Jy}$ .

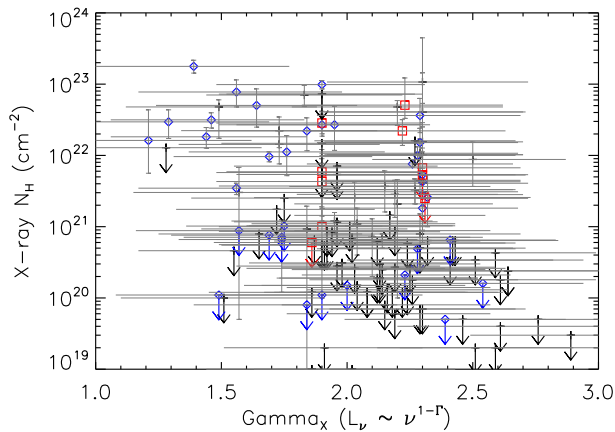


FIG. 1.— The column density  $N_H$  and the X-ray slope  $\Gamma_X$  measured from the X-ray spectrum for the 153 AGNs with  $> 40$  XMM or Chandra counts. X-ray slope  $\Gamma_X$  is defined by  $L_\nu \propto \nu^{1-\Gamma_X}$ . Black crosses show broad-line AGNs, blue diamonds show narrow-line AGNs, and red squares show lineless (optically dull) AGNs. The median X-ray slope for all AGNs is  $\Gamma_X = 2.1$ , although  $\Gamma_X$  ranges from 1 to 3. There are 118 unobscured AGNs with  $N_H < 10^{22} \text{cm}^{-2}$ .

### 3. CHARACTERIZING AGN SPECIFIC ACCRETION RATE

In this work we describe the specific accretion rate using the Eddington ratio parameter,  $\lambda \equiv L_{int}/L_{Edd}$ . Here  $L_{int}$  is the intrinsic luminosity, a measure of the total accretion luminosity which includes only light from the accretion disk and X-ray corona and excludes any reprocessed IR emission. While the reprocessed IR emission can represent a large fraction of the bolometric luminosity, especially for obscured AGNs, it may be anisotropic. Most of our AGNs are unobscured (see Section 2.1) and we exclude the IR emission to avoid double-counting

the AGN emission. Instead we use only the optical/UV and X-ray emission which comes directly from the disk and corona in the AGN: in this work when using “intrinsic” luminosity we are always referring to the total of the disk (optical/UV) and corona (X-ray) emission, without the reprocessed (IR) emission. The Eddington luminosity is derived from the black hole mass, with  $L_{Edd} = 1.3 \times 10^{38} (M_{BH}/M_\odot) \text{erg s}^{-1}$ . AGN luminosity is powered by accretion rate, with  $L_{int} = \eta \dot{M} c^2$ . For a constant efficiency  $\eta$ , the Eddington ratio  $\lambda$  is equivalent to the specific accretion rate  $\dot{m} \equiv \dot{M}/\dot{M}_{Edd}$ . For example, assuming  $\eta \sim 0.1$  the Eddington accretion rate can be written  $\dot{M}_{Edd} = 5 M_8 M_\odot \text{yr}^{-1}$  with  $M_8 = M/(10^8 M_\odot)$ . However there is good evidence that  $\eta$  decreases at very low accretion rates  $\dot{m} \ll 0.01$  (e.g., Narayan & McClintock 2008). Indeed, in Sections 4 and 5 we invoke a lower-efficiency (radiatively inefficient) accretion to explain the observational properties of  $L_{int}/L_{Edd} < 10^{-2}$  AGNs. This means that the accretion power  $L_{int}/L_{Edd}$  probably underestimates the accretion rate  $\dot{m}$  for our most weakly accreting AGNs with  $L_{int}/L_{Edd} < 10^{-2}$ : e.g., a measured accretion power of  $L_{int}/L_{Edd} \sim 10^{-4}$  might correspond to  $\dot{m} \sim 10^{-3}$ .

Below we outline our methods for estimating black hole masses and bolometric luminosities from the data for the AGNs in our sample. Table 2 presents the full catalog of  $L_{int}$ ,  $M_{BH}$ , and  $L_{int}/L_{Edd}$ , and their associated errors, for our AGNs.

#### 3.1. Intrinsic Luminosity Estimates

We calculate the intrinsic luminosity from the full rest-frame near-IR to X-ray multiwavelength data. This avoids monochromatic bolometric corrections which are highly uncertain and probably depend on Eddington ratio (e.g., Kelly et al. 2008; Vasudevan & Fabian 2009).

Instead we measure intrinsic luminosity by integrating the best-fit accretion disk + X-ray power-law SED model. We compile the broad-band near-IR ( $K_s, J$ ), optical ( $z^+, r^+, i^*, g^+, V_J, B_J, u^*$ ), UV (GALEX NUV & FUV), and X-ray (0.5-2 keV and 2-10 keV from Chandra when available or XMM-Newton) data, for which the wavebands and limits are described in Table 1. To avoid reprocessed mid-IR emission, which would double-count the intrinsic emission for an unobscured AGN, we restrict the accretion disk fit to rest-frame  $1 < E < 100$  eV ( $6200 > \lambda > 124$  Å). The radio emission is negligible in the total energy output of our AGNs. While narrow-band optical photometry also exists for our AGNs, its inclusion doesn't appreciably change the best-fit multi-wavelength SED from using only the broad-band data.

The rest-frame near-IR and optical emission of narrow-line and lineless AGNs is dominated by the emission from the host galaxy. For these objects, accurate intrinsic luminosities require modeling and subtracting the host galaxy light. Gabor et al. (2009) measured the host F814W luminosities from surface brightness fitting to the HST/ACS data of our AGNs. We use this luminosity to scale a galaxy template from Polletta et al. (2007). Lineless AGNs have early-type hosts, since their spectra lack the emission lines associated with a late-type star-forming galaxy, and so we use the “Ell5” early-type template from Polletta et al. (2007). The narrow-line galaxies in our sample typically have intermediate-type (“green valley”) hosts based on their morphologies (Gabor et al. 2009) and star formation rates (Silverman et al. 2009), and so we use the “S0” template of Polletta et al. (2007). We subtract the host contribution in each photometric band before performing our SED fit. The reddest (“Ell2”) and bluest (“Sd”) normal galaxy templates of Polletta et al. (2007) are additionally used as extreme hosts to estimate the possible error contribution from choosing the wrong host template (described in §3.3).

It is possible that a few of the narrow-line and lineless AGNs might have very blue starbursting hosts, although such galaxies are uncommon at  $z < 1$ . An extremely blue, UV-emitting host would cause us to overestimate the accretion disk emission and consequently overestimate the accretion rate. Since the narrow-line and lineless AGNs have lower accretion rates than broad-line AGNs (as we discuss in Section 4), if their true accretion rates were even lower it would only strengthen our conclusions. It is also possible that very red, dusty hosts could cause us to underestimate the true accretion rates for narrow-line and lineless AGNs. However a dusty host should cause the AGN to appear extinguished, and our sample of AGNs generally has low measured absorption (see Section 2.1). In addition, restricting our fitting to  $1 < E < 100$  eV ( $6200 > \lambda > 124$  Å) already means that a normal elliptical galaxy (like our “Ell2” template) contributes very little flux where we fit the accretion disk.

While broad-line AGNs are likely to have some host contribution, we cannot use surface brightness fitting to estimate their host luminosity because they are at high redshift and their point source overwhelms their extended emission (Gabor et al. 2009). However at the peak of the accretion disk emission for a broad-line AGN ( $\sim 3000$ Å, or 4 eV) the host galaxy contributes

$< 20\%$  of the emission (e.g., Bentz et al. 2006). Because we additionally restrict our accretion disk fitting to  $1 < E < 100$  eV ( $6200 > \lambda > 124$  Å), we can assume that the error from not subtracting the host for broad-line AGNs is typically  $< 0.1$  dex.

We shift the observed (and host-subtracted, for narrow-line and lineless AGNs) photometry to the rest-frame from the measured spectroscopic redshift and convert the magnitudes or fluxes to luminosities. We then fit an accretion disk model to the optical/UV emission within the range  $1 < E < 100$  eV ( $4.8 \times 10^{14} < \nu < 2.4 \times 10^{16}$  Hz, or  $6200 > \lambda > 124$  Å) and a power-law representing the X-ray corona emission to the rest-frame X-ray data. We measure the total bolometric luminosity from the sum of the disk luminosity (given by the analytic solution in Equation 3 below) and the power-law luminosity from  $4E_{peak} < E < 250$  keV (where  $E_{peak}$  is the peak energy of the best-fit disk model). While the X-ray background requires a high-energy cutoff for AGNs in the few hundreds of keV (Gilli et al. 2007), measurements of the cutoff energy exist for only  $\sim 15$  AGNs and vary from 50-500 keV (Perola et al. 2002; Molina et al. 2006). We choose 250 keV as an intermediate value, although any cutoff from 50-500 keV does not greatly influence our results. Our AGNs have typically flat X-ray spectra with  $\Gamma_X \sim 2$ , and so changing the X-ray cutoff energy by a factor of 0.2-2 effectively changes the integrated X-ray luminosity by the same factor of a few. Because the X-ray and disk luminosities are roughly comparable (see Figure 2), this results in less than a factor of two change in the total accretion luminosity: much less than the  $\sim 0.5$  dex errors we compute for our estimated  $L_{int}/L_{Edd}$  (see §3.3).

We use the accretion disk model of Gierliński et al. (1999), which improves upon a basic blackbody accretion disk by including a correction for relativistic effects. (The Gierliński et al. (1999) model is the “diskpn” model of the XSpec X-ray fitting software.) This model is based on the pseudo-Newtonian gravitational potential  $\Phi = -GM/(R - R_g)$  (Paczynski & Wiita 1980), where  $R_g$  is the Schwarzschild radius  $R_g = GM/c^2$ . From Gierliński et al. (1999), the model takes the form:

$$L = KE^4 \int_{r_{in}}^{\infty} \frac{r dr}{\exp[E/kT(r)] - 1} \quad (1)$$

where  $r = R/R_g$  and we assume the innermost stable orbit  $r_{in} = 6$ . The temperature depends on radius as

$$T(r) = \frac{T_0}{c_0} \left[ \frac{r - 2/3}{r(r - 2)^3} \left( 1 - \frac{3^{3/2}(r - 2)}{2^{1/2}r^{3/2}} \right) \right]^{1/4}, \quad (2)$$

with  $c_0 \simeq 0.1067$ , and  $T_0 \propto m^{-1/4} \dot{m}^{1/4}$ . The coefficient  $K$  depends on inclination angle, coronal absorption, and the color to effective temperature ratio. Rather than estimate these values, we assume that  $K$  is a constant, computed by simply scaling the model to our data.  $T_0$  is the sole free parameter. In our analyses below we refer to  $E_{peak}$ , the peak energy of the disk, rather than  $T_0$ , and in general  $kT_0 \simeq E_{peak}/24$ . We find the best-fit disk model in terms of  $T_0$  by minimizing the  $\chi^2$  function. While most of the best-fit disk models have significant emission at  $E < 1$  eV, we restrict the fit to  $1 < E < 100$  eV to

mitigate the effects of a contaminating torus and/or host galaxy light.

Note that the relation  $T_0 \propto m^{-1/4}\dot{m}^{1/4}$  above means that the disk temperature is constrained not only by the photometry but also by the black hole mass. In practice this prevents our fits from resulting in unphysically hot accretion disks, since disks peaking at energies much higher than  $\sim 4$  eV ( $3000\text{\AA}$ ) would require unphysically small black hole masses. This is especially important to note because about one-third of the sample lacks GALEX UV detections, and as a result the declining high-energy slope is not well constrained by the photometry for low redshift AGNs. The black hole mass error ( $\sim 0.4$  dex) is used during the bootstrapped uncertainty measurements for the accretion disk temperature and luminosity.

The total disk luminosity is calculated analytically (see Appendix A of Gierliński et al. 1999):

$$L_{disk} = K \frac{h^3 c^2}{16\pi} \left( \frac{T(r_{in})}{c_0} \right)^4. \quad (3)$$

Errors in both  $E_{peak}$  and  $L_{disk}$  are found by bootstrapping 1000 fits to the resampled data.

To characterize the X-ray corona emission, we use the X-ray spectral fits described in §2.1. Each X-ray spectrum is fit as an intrinsically absorbed power-law with Galactic absorption ( $N_{H,gal} = 2.6 \times 10^{20} \text{ cm}^2$  in the direction of the COSMOS field). We use the photon index  $\Gamma_X$  to represent the power-law slope, such that  $L_\nu = L_0 \nu^{1-\Gamma}$ . Figure 1 shows that the typical  $\Gamma_X \simeq 1.9 \pm 0.4$ , and we assume this slope for AGNs with too few X-ray counts for a good fit. We calculate the total X-ray luminosity by integrating the power-law model over  $4E_{peak} < E < 250 \text{ keV}$  (where  $E_{peak}$  is the energy peak of the disk model), using the analytic solution:

$$L_X = L_0 / (2 - \Gamma) \times [(250 \text{ keV} / h)^{2-\Gamma} - (4E_{peak} / h)^{2-\Gamma}] \quad (4)$$

The total bolometric luminosity is simply the sum of the integrated accretion disk and X-ray power-law components,  $L_{int} = L_{disk} + L_X$ .

Figure 2 shows a representative sample of broad-line, narrow-line, and lineless SEDs with model fits. Note that emission lines and variability (the various photometric data were taken over 3 years) mean that our simple accretion disk model is not a perfect fit: some of the optical/UV data and differ from the model fit by up to 0.2 dex. However, such small errors in individual photometry points are negligible compared to the  $> 0.4$  dex total errors we estimate for  $L_{int}$  (see Figure 4 and Section 3.3). In general, the accretion disk plus X-ray power-law model provides an accurate, physically motivated fit to the data.

### 3.2. Black Hole Mass Estimates

For Type 1 AGNs, we estimate black hole masses using the scaling relations of Vestergaard & Osmer (2009) for the MgII broad emission line and Vestergaard & Peterson (2006) for the H $\beta$  and CIV broad emission lines. These relations estimate black hole mass from single-epoch spectra by employing the correlation between the radius of the broad emission line region and the continuum luminosity,

$R_{BLR} \sim L^{0.5}$ , observed in local AGN with reverberation mapping (Bentz et al. 2006; Kaspi et al. 2007). In general, masses estimated from the scaling relations are accurate to  $\sim 0.4$  dex (Vestergaard & Peterson 2006; Shen et al. 2008) and agree with local AGN masses from dynamical estimators (Davies et al. 2006; Onken et al. 2007) and the  $M_{BH}$ - $\sigma^*$  correlation (Onken et al. 2004; Greene & Ho 2006). The scaling relations take the form of Equation 5, with  $\lambda L_\lambda$  in units of  $10^{44} \text{ erg/s}$  and  $v_{FWHM}$  in units of 1000 km/s;  $A = 6.91$ ,  $B = 0.50$ , and  $\lambda = 5100\text{\AA}$  for H $\beta$ ;  $A = 6.86$ ,  $B = 0.50$ , and  $\lambda = 3000\text{\AA}$  for MgII;  $A = 6.66$ ,  $B = 0.53$ , and  $\lambda = 1350\text{\AA}$  for CIV.

$$\log \left( \frac{M_{BH}}{M_\odot} \right) = A + B \log(\lambda L_\lambda) + 2 \log(v_{FWHM}) \quad (5)$$

Black hole masses for the Type 1 AGNs with Magellan/IMACS or SDSS spectra in COSMOS are already published in previous work (Trump et al. 2009b), and we repeat the same techniques for Type 1 AGNs with VLT/VIMOS spectra. Briefly, a power-law fit plus iron emission are fit to each AGN. The continuum luminosity is estimated directly from the continuum fit, while the velocity widths are computed from Gaussian fits to the continuum-subtracted emission lines. Some objects also have black hole masses from Merloni et al. (2010); for these objects, our masses are consistent with a random scatter of only  $\sim 0.4$  dex: equivalent to the intrinsic scatter of the scaling relations (see Figure 3 of Trump et al. 2009b). Marconi et al. (2008) showed that the scatter in  $M_{BH}$  from the scaling relations might decrease to 0.2 dex if radiation pressure is taken into account. Replacing the scaling relations from Equation 5 with those of Marconi et al. (2008) would tighten the distribution of  $L_{int}/L_{Edd}$  estimates for broad-line AGNs about  $L_{int}/L_{Edd} \sim 0.3$ . This has no impact on the  $M_{BH}$  estimates for narrow-line and lineless AGNs, and does not affect the difference in  $L_{int}/L_{Edd}$  between the broad-line sample and the narrow-line and lineless AGN sample.

Estimating black hole masses for AGNs without broad emission lines requires secondary estimators. We employ the relationship between  $M_{BH}$  and rest-frame  $K$ -band host bulge luminosity (Graham 2007):

$$\log \left( \frac{M_{BH}}{M_\odot} \right) = 0.93(\log(L_K) - 0.3z) - 32.30, \quad (6)$$

with  $L_K$  in units of  $\text{erg s}^{-1}$ . The  $M_{BH} - L_{K,bulge}$  relation comes from the more fundamental  $M_{BH} - M_*$  relation, since rest-frame  $K$  bulge luminosity is correlated with  $M_*$  (e.g., Ilbert et al. 2010). We add an additional  $-0.3z$  term to the (Graham 2007) relation in order to account for the evolution in the  $M_*/L_K$  ratio,  $\log(M_*/L_K) \propto -0.3z$  (Arnouts et al. 2007). We measure rest-frame  $L_K$  from the host galaxy template from the multiwavelength SED fit (described above in §3.1). The early-type template for the lineless AGNs is, by definition, bulge-dominated, and so  $L_{K,bulge} = L_{K,host}$ . The S0 template used for the narrow-line AGNs, however, has a significant disk component, and so we take  $L_{K,bulge} = 0.5L_{K,host}$ . The intrinsic error in the  $M_{BH} - L_K$  is 0.35 dex (Graham 2007). We do not correct the  $M_{BH}$  estimates for any evolution in the  $M_{bulge} - M_{BH}$  relation because mea-

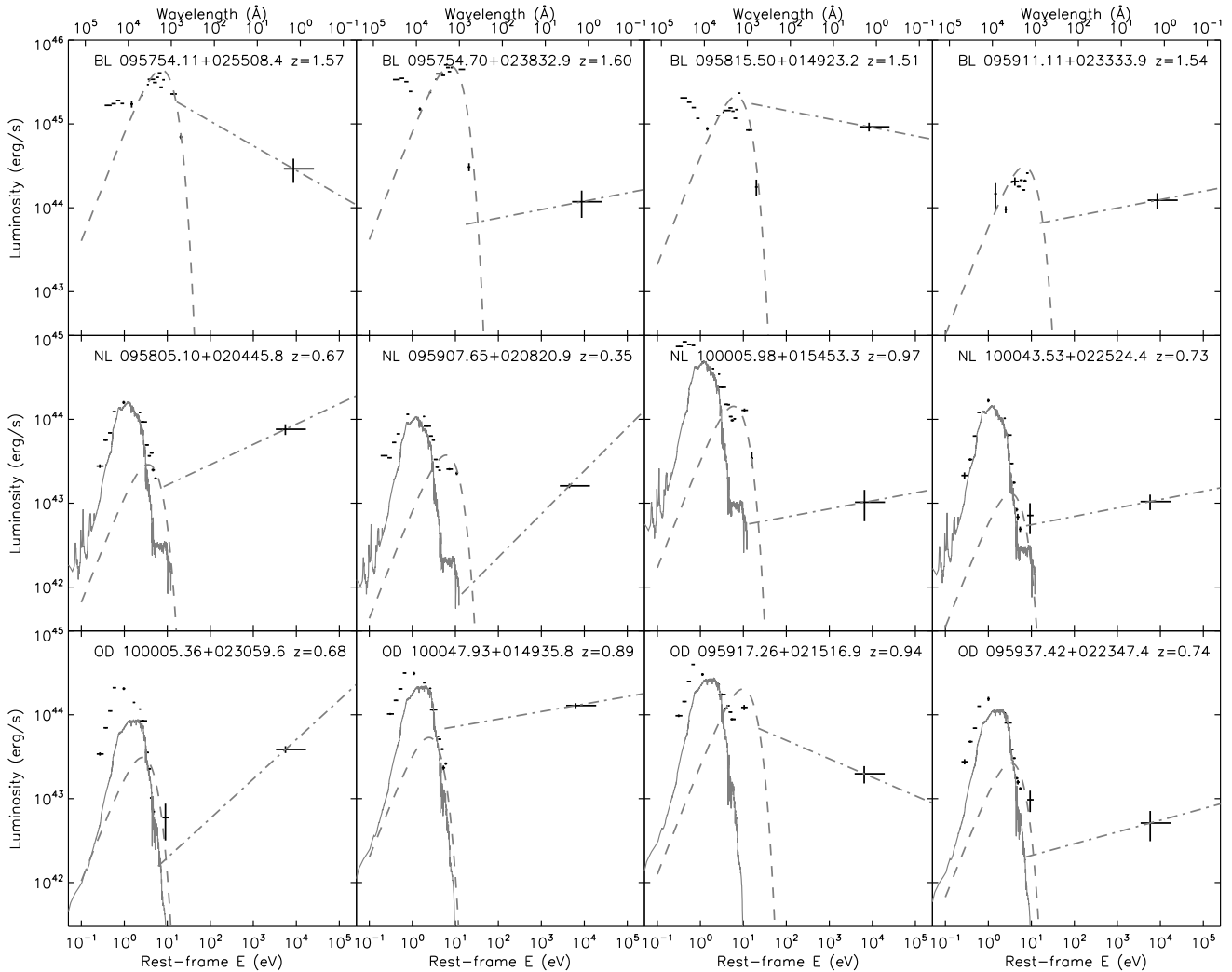


FIG. 2.— Multiwavelength photometry and model fits for 12 example AGNs. The top four panels are broad-line AGNs (represented by ‘BL’), the middle four are narrow-line AGNs (represented by ‘NL’), and the bottom four are lineless “optically dull” AGNs (represented by ‘OD’). In each panel, the dashed line is the best-fit accretion disk model and the dot-dashed line is the X-ray power-law fit. The X-ray power-law slope comes from the X-ray spectral fit, although we show only the X-ray photometry data in this figure. Estimated host SEDs are shown by solid lines for the narrow-line and lineless AGNs. We fit only at  $E > 1$  keV in order to ignore the reprocessed IR emission, and so the longest-wavelength photometry data (especially the IRAC channels) are not fit by our models.

suring of  $M_{\text{bulge}} - M_{\text{BH}}$  evolution has proved difficult due to significant biases in most tests (Lauer et al. 2007; Shen & Kelly 2010). Besides, while there is some evidence for evolution to  $z \sim 3$  (Decarli et al. 2010), there is probably little or no evolution to  $z \sim 1.5$  (Jahnke et al. 2009) and our narrow-line and lineless AGNs lie at  $z < 1$ .

Because we use different mass estimators for broad-line and narrow-line/lineless AGNs, it is important to demonstrate that the two methods agree. Seven of our broad-line AGNs have detected host galaxies from the decompositions of Gabor et al. (2009), and for these AGNs we compare  $M_{\text{BH}}$  estimates from the broad-line scaling relations and from the host galaxy rest-frame  $L_K$  in Figure 3. The  $M_{\text{BH}}$  estimates from broad lines and  $L_K$  agree within  $< 2\sigma$  for all objects (indeed, estimates for all objects but one agree within  $< 1\sigma$ ). In addition to the seven broad-line AGNs in our sample, both the broad-line and host galaxy  $M_{\text{BH}}$  estimators have been shown to produce consistent masses for nearby AGNs (Onken et al. 2004; Greene & Ho 2006). It is particularly unlikely that either of the estimators is systematically off by a factor of 100.

Therefore we are confident that the factor of 100 difference in  $L_{\text{int}}/L_{\text{Edd}}$  for broad-line and narrow-line/lineless AGNs in Section 4 (see, for example, Figure 5) is a physical effect, robust beyond the choice of black hole mass estimator.

We highlight the range and limitations of the AGN sample in Figure 4, which shows bolometric luminosities and black hole masses for the broad-line, narrow-line, and lineless AGNs. Objects in the upper left have the highest specific accretion rates, while those in the lower right are weakly accreting AGNs. While the total sample spans 3 orders of magnitude in both luminosity and black hole mass, our narrow-line and lineless AGNs are generally less luminous and more massive than broad-line AGNs. The lack of low-mass narrow-line and lineless AGNs is due to the selection limits of the survey: such objects are too faint to be detected in COSMOS. It is suggestive that these higher mass narrow-line and lineless AGNs are at  $z < 1$  and are less luminous: this is consistent with “downsizing,” with more massive AGNs becoming less active at lower redshift (Ueda et al. 2003;

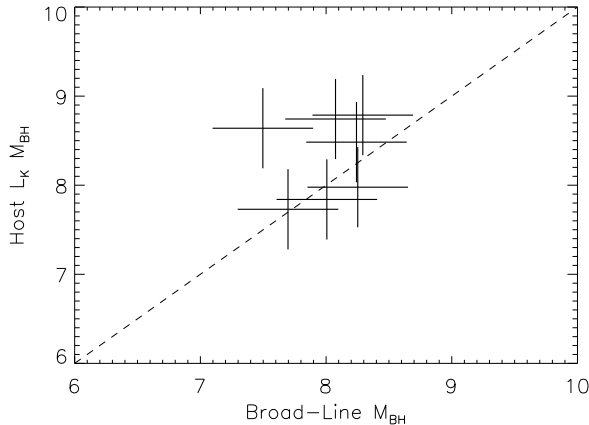


FIG. 3.— Black hole mass estimates from both the host  $L_K$  and the broad-line scaling relations for the seven broad-line AGNs with detected host galaxies from Gabor et al. (2009). For all but one AGN, both  $M_{BH}$  estimates agree within  $\lesssim 1\sigma$  (for the remaining object, the two estimates differ by only  $\sim 2\sigma$ ). From these AGNs, and the sets of nearby AGNs with similarly consistent masses from both estimators (Onken et al. 2004; Greene & Ho 2006), it is unlikely that the different mass estimators cause bias between broad-line and narrow-line/lineless AGNs.

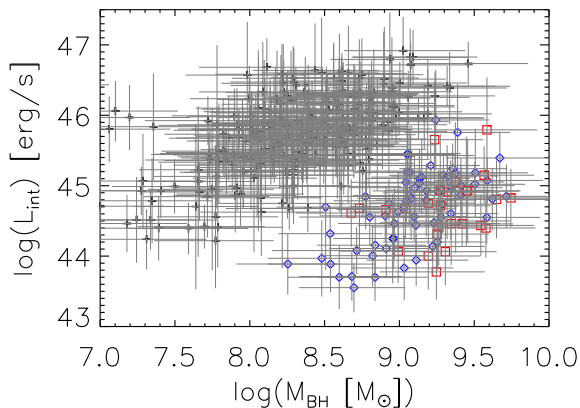


FIG. 4.— Intrinsic luminosity  $L_{int}$  with black hole mass  $M_{BH}$  for the AGN sample. Broad-line AGNs are shown by black crosses, narrow-line AGNs by blue diamonds, and lineless AGNs by red squares. Errors are calculated as described in Section 3.3. Narrow-line and lineless AGNs generally have higher mass, due to the COSMOS selection limits, but they also have lower luminosities as expected by downsizing.

Brandt & Hasinger 2005; Bongiorno et al. 2007).

Figure 4 shows that at a given mass or luminosity there are generally all types of AGNs present in our sample. For this reason we do not expect that the differences between broad-line and narrow-line/lineless AGNs are biased by selected samples from different masses or luminosities. In addition, despite the different redshifts of most broad-line and narrow-line/lineless AGNs, we do not expect their differences to be caused by redshift. There is evidence that AGN obscuration properties depend on redshift (Treister et al. 2009; Trump et al. 2009a), but these AGNs are unobscured. The AGN central engine, meanwhile, does not change with redshift in terms of ionization parameters (Dietrich & Hamann

2004; Vestergaard 2004), spectral energy distributions (Vignali et al. 2003; Richards et al. 2006; Kelly et al. 2008), or metallicity (Simon et al. 2010). Limiting the sample to  $z < 1$ ,  $8.5 < \log(M_{BH}) < 9$ , or  $44 < \log(L_{int}) < 45$  does not significantly change the differences between the broad-line and narrow-line/lineless AGN samples seen in Figures 5, 6, 7, or 8.

### 3.3. Error Budget

We estimate errors for each of our specific accretion rates, propagating the errors from both the intrinsic luminosity estimate and the black hole mass estimate. Our intrinsic luminosity is subject to three major uncertainties:

- Photometry errors,  $\sigma_{phot}$ . We measure the error contribution of the photometry by bootstrapping, fitting our model SED to 1000 realizations of randomly drawn photometry values distributed according to the measurement errors. In general,  $\sigma_{phot} \sim 0.1$  dex.
- Errors in the host subtraction,  $\sigma_{host}$ . For broad-line AGN, we do not subtract a host component and assume that any remaining galaxy light overestimates the intrinsic luminosity (from the UV and X-ray) by only  $< 0.1$  dex (see §3.1). For narrow-line and lineless AGN we estimate  $\sigma_{host}$  from the difference in the resultant  $L_{int}$  when using a very red (“E112”) and a very blue (“Sd”) template from Polletta et al. (2007). Since the accretion disk is fit only at  $E > 1$  eV where there is little host emission (even from the “Sd” galaxy), this error is usually insignificant ( $\sigma_{host} \lesssim 0.1$  dex).
- Incorrect  $L_{int}$  resulting from extinction,  $\sigma_{ext}$ . Extinction will make the true  $L_{disk}$  greater than our estimate because optical/UV light will be missed, but will make the true  $L_X$  lower than our estimate because the power-law slope will be too hard. Because we restrict our main analyses to unobscured ( $N_H < 10^{22} \text{ cm}^{-2}$ ) AGNs, we assume this error is  $< 0.1$  dex (see §2.1).

The black hole estimate is subject to two major uncertainties:

- Intrinsic errors in the  $M_{BH}$  relations,  $\sigma_{rel}$ . For broad-line AGN, the intrinsic error in the scaling relations is 0.4 dex (Vestergaard & Peterson 2006), such that  $\sigma_{rel} = 2.5M_{BH}$ . For narrow-line and lineless AGN, we use the  $M_{BH} - L_{K,host}$  relation, and its associated intrinsic scatter is 0.35 dex (Graham 2007), such that  $\sigma_{rel}/M_{BH} = 2.2$ . These errors dominate the error in  $L_{int}/L_{Edd}$ , except for highly absorbed AGNs with  $N_H > 10^{22.5} \text{ cm}^{-2}$ .
- Measurement error in the luminosity used in the scaling relation,  $\sigma_{lum}$ . For broad-line AGN, this is the measured continuum luminosity associated with the appropriate scaling relation, estimated by Trump et al. (2009b) as  $\sigma_{lum} \sim 0.05$  dex. Since  $M_{BH} \propto L^{0.5}$ ,  $\sigma_{lum} = 1.3M_{BH}$  for broad-line AGNs. For other AGNs the  $\sigma_{lum}$  comes from our measured  $L_{K,rest}$ . We estimate this error for the



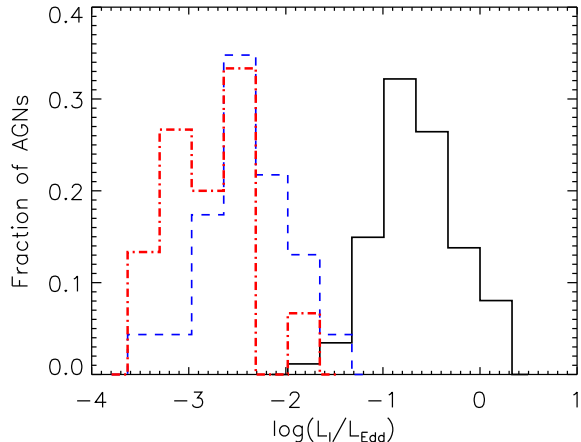


FIG. 5.— The distribution of calculated specific accretion rates ( $L_{int}/L_{Edd}$ ), for the 82 unobscured ( $N_H < 10^{22} \text{ cm}^{-2}$ ) broad-line AGNs (black histogram), 24 narrow-line AGNs (blue dashed histogram), and 12 lineless AGNs (red dotted histogram). Narrow-line and lineless AGNs have significantly lower accretion rates than broad-line AGNs. The  $L_{int}/L_{Edd} \gtrsim 0.01$  limit for broad-line AGNs is not a selection effect (Trump et al. 2009b).

narrow-line and lineless AGNs from 1000 fits to the randomly subsampled data, and find that the error is generally insignificant compared to the intrinsic error ( $\sigma_{lum} \sim 0.05$  dex). Note the contribution from error in  $v_{FWHM}$  to  $M_{BH}$  in broad-line AGNs is also negligible, since for our AGNs  $\sigma(v_{FWHM}) < 0.2v_{FWHM}$  (Trump et al. 2009b).

The total error in specific accretion rate,  $\sigma_\lambda$ , is then given by:

$$\frac{\sigma_\lambda^2}{\lambda^2} = \frac{\sigma_{phot}^2 + \sigma_{host}^2}{L_{int}^2} + \frac{\sigma_{rel}^2 + \sigma_{lum}^2}{M_{BH}^2} \quad (7)$$

We measure the total error  $\sigma_\lambda$  by bootstrapping, with 1000 fits to the resampled data. In each fit we allow all of the parameters above to vary according to their error. The intrinsic error in the  $M_{BH}$  relations ( $\sigma_{rel}$ ) dominates the error. The average errors are  $\sim 0.5$  dex, compared to the  $\sim 4$  dex range in  $L_{int}/L_{Edd}$  for the AGN in the sample.

#### 4. THE PHYSICAL EFFECTS OF SPECIFIC ACCRETION RATE

The distribution of  $L_{int}/L_{Edd}$  for the 118 unobscured AGNs is shown in Figure 5. It is immediately evident that unobscured narrow-line and lineless AGNs accrete much more weakly than broad-line AGNs, with specific accretion rates differing, on average, by  $\sim 2$  orders of magnitude. This suggests that many narrow-line and lineless AGNs are not simply geometrically obscured versions of broad-line AGNs, but they instead have fundamentally different accretion physics which we examine in more detail below.

The large  $\sim 0.5$  dex errors in accretion rate artificially broaden the distributions, such that the intrinsic distributions are likely to be narrower than the histograms in Figure 5 appear (although many  $L_{int}/L_{Edd} \lesssim 10^{-3}$  narrow-line and lineless AGNs could be too faint for the COSMOS X-ray and spectroscopy limits). The

$L_{int}/L_{Edd} \gtrsim 0.01$  limit for broad-line AGNs could be partially explained by selection effects (Kelly et al. 2010), since low accretion rate AGNs are typically less luminous. However at the highest masses ( $M_{BH} \sim 10^9 M_\odot$ ), broad-line AGNs with  $L_{int}/L_{Edd} \lesssim 0.01$  must be very rare (Kollmeier et al. 2006; Trump et al. 2009b). Meanwhile unobscured narrow-line and lineless AGNs are generally limited by  $L_{int}/L_{Edd} \lesssim 0.01$ . With low X-ray column densities and low accretion rates, these objects have similar properties to the “naked” Type 2 AGNs of Tran (2003), which additionally lack reflected broad emission lines in spectropolarimetry (see also Gliozzi et al. 2007; Wang & Zhang 2007). We expect that the X-ray unobscured low accretion rate AGNs would similarly lack reflected broad emission lines. Our method cannot accurately estimate  $L_{int}/L_{Edd}$  for obscured AGNs, but following a unified model with geometric obscuration (e.g., Antonucci 1993), obscured narrow-line AGNs would likely have accretion rates comparable to our broad-line AGNs.

We can compare the specific accretion rates and AGN types with the physical parameters of our model fits: namely the ratio of disk to power-law emission, the peak energy of the accretion disk model, and the X-ray power-law slope. These quantities are particularly useful in unifying AGN in terms of their accretion physics. Figure 6 shows the specific accretion rate with these parameters for each AGN type. The values of  $L_{disk}/L_X$  can be roughly translated to values of  $\alpha_{OX}$ , with  $\alpha_{OX} = -0.384 \log[L_\nu(2500\text{\AA})/L_\nu(2\text{keV})]$  (Tananbaum et al. 1979; Kelly et al. 2008). The left panel of Figure 6 shows tracks of  $\alpha_{OX} = 1.0, 1.5, 2.0$ , assuming  $E_{peak} = 6$  keV and  $\Gamma_X = 1.9$  (hotter disks and softer X-ray slopes increase  $\alpha_{OX}$ ). Once again, narrow-line and lineless AGNs have lower specific accretion rates, and they also tend to have lower  $L_{disk}/L_X$  and  $E_{peak}$ .

We can determine the significance of any differences in  $L_{disk}/L_X$ ,  $E_{peak}$ , and  $\Gamma_X$  between rapidly accreting broad-line AGNs and weakly accreting narrow-line and lineless AGNs by comparing their mean values and considering the scatter of each sample. Given mean values  $\mu_1$  and  $\mu_2$  and associated scatters  $\sigma_1$  and  $\sigma_2$  for each set, the significance of their difference is given by  $(\mu_1 - \mu_2)/\sqrt{(\sigma_1^2/N_1 + \sigma_2^2/N_2)}$  (where  $N_1$  and  $N_2$  are the numbers of AGNs in each sample). The broad-line AGNs have  $\mu(\log(L_{disk}/L_X)) = -0.14 \pm 0.44$  while the narrow-line and lineless AGNs have  $\mu(\log(L_{disk}/L_X)) = -0.38 \pm 0.64$ , so that their difference is marginally significant at  $2.1\sigma$ . The difference in  $E_{peak}$  is more significant: the broad-line AGNs have  $\mu(\log(E_{peak})) = 0.80 \pm 0.20$  and the narrow-line/lineless AGNs have  $\mu(\log(E_{peak})) = 0.59 \pm 0.37$ , so that the difference is significant to  $3.3\sigma$ . From this we can conclude that a transition from weakly accreting narrow-line and lineless AGNs to the rapidly accreting broad-line AGNs results in significantly hotter and marginally brighter emission from the accretion disk.

There is no significant difference between X-ray slope  $\Gamma_X$  for the different AGN types: mean  $\Gamma_X = 2.14 \pm 0.29$  for rapidly accreting broad-line AGNs, and mean  $\Gamma_X = 2.05 \pm 0.29$  for weakly accreting narrow-line and lineless AGNs (the difference is only  $1.2\sigma$  significant). This is in contrast to the prediction of Hopkins et al. (2009), who suggest that harder X-ray slopes are expected for radia-

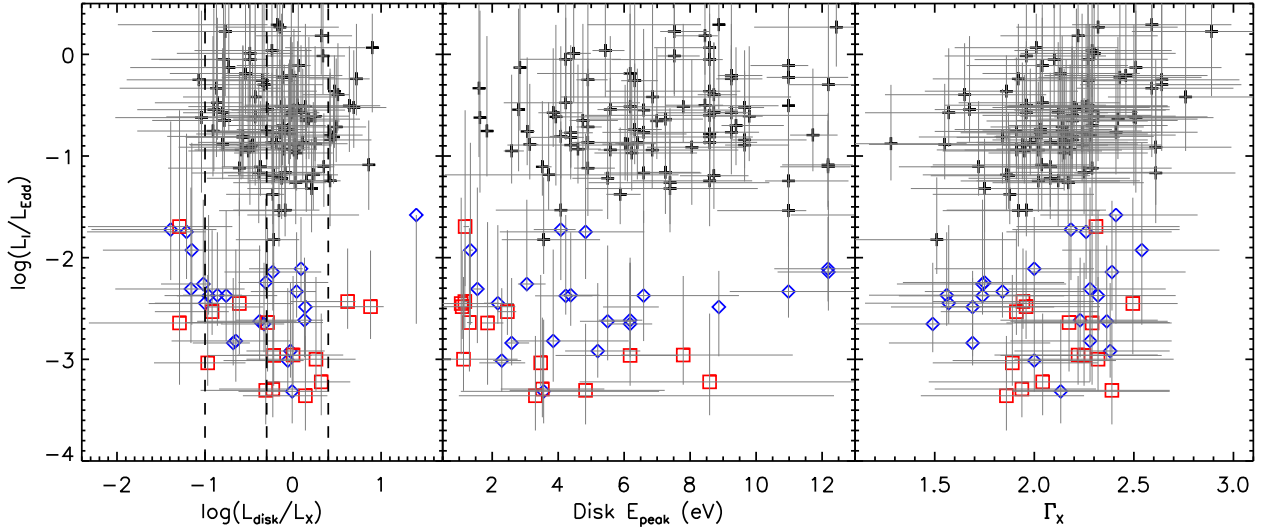


FIG. 6.— Specific accretion rate  $L_{int}/L_{Edd}$  and the ratio of disk to corona emission  $\log(L_{disk}/L_X)$ , disk temperature  $E_{peak}$  and X-ray photon index  $\Gamma_X$  for the 118 unobscured AGNs with  $N_H < 10^{22} \text{ cm}^{-2}$ . In each panel, black crosses represent broad-line AGNs, blue diamonds are narrow-line AGNs, and red squares are lineless AGNs. The dashed lines in the left panel show lines of  $\alpha_{OX} = 1.0, 1.5, 2.0$ , assuming  $E_{peak} = 6 \text{ keV}$  and  $\Gamma_X = 1.9$ . Unobscured narrow-line and lineless AGNs have  $\sim 100$  times lower accretion rates than broad-line AGNs, as well as significantly cooler and somewhat weaker accretion disks.

tively inefficient accretion flows (RIAF) expected at low accretion rates. The appearance of a RIAF at inner radii might produce more X-ray emission, as we discuss in §4.1 below, but this emission probably has a similar power-law slope as the X-ray corona present in broad-line AGNs with high accretion rates. This is unsurprising, since both the RIAF and the corona are thought to be ionized plasmas with X-ray emission from inverse Compton scattering and/or bremsstrahlung. We can conclude that the onset of a RIAF in unobscured narrow-line and lineless AGNs with accretion rates of  $10^{-4} < L_{int}/L_{Edd} < 10^{-2}$  do not cause harder X-ray power-law slopes.

#### 4.1. Physics of the Accretion Disk

As accretion rate increases from lineless and narrow-line to broad-line AGNs, the disk temperature significantly increases and its brightness with respect to the X-rays marginally increases. An increase in temperature with accretion rate is expected for a thin accretion disk, which has  $T_{max} \propto \dot{m}^{1/4}$  (Shakura & Sunyaev 1973). We additionally discuss below how the onset of a radiatively inefficient accretion flow could also cause apparent cooler disk emission. Both an increase in temperature and in  $L_{disk}/L_X$  with accretion rates would contribute to the observed increase of  $\alpha_{OX}$  (the ratio of rest-frame UV to X-ray emission) with accretion rate (Kelly et al. 2008; Young et al. 2010). In our previous work (Trump et al. 2009c), we suggested that the increase of  $\alpha_{OX}$  with accretion rate was due only to the disk luminosity decreasing with respect to the corona luminosity. While this is partly correct, the correlation is also caused by increasing disk temperatures at higher accretion rates.

AGNs with  $L_{int}/L_{Edd} \lesssim 0.01$  are predicted to have radiatively inefficient accretion flows (RIAFs) near the central black hole (Begelman, Blandford & Rees 1984; Narayan et al. 1995; Yuan 2007; Narayan & McClintock 2008). At such accretion rates, we can define a truncation radius  $R_t$  where the collisional cooling time is

comparable to the accretion time. Beyond  $R_t$ , accretion will remain in a standard geometrically thin and optically thick disk with a thermal blackbody spectrum (e.g., Shakura & Sunyaev 1973). However within  $R_t$ , there are too few collisions to couple the ions and electrons and the gas becomes a two-temperature plasma. The electrons are cooled by bremsstrahlung, synchrotron, and Compton up-scattering, while the ions remain at the virial temperature. This means the flow is geometrically thick and optically thin. The introduction of a truncation radius changes the  $R_{in} = 6R_g$  assumption for the accretion disk model, since by definition  $R_{in} \geq R_t$ . The peak energy of the best-fit accretion disk model is not very sensitive to the choice of  $R_{in}$ , although larger inner radii change the shape of the model with additional red emission. At accretion rates  $L_{int}/L_{Edd} \gtrsim 10^{-3}$ , as in our sample,  $R_t \sim 80R_g$  (Yuan & Narayan 2004). Using  $r_{in} = 80$  in the accretion disk model fitting in Section 3.1 doesn't change the best-fit values of  $E_{peak}$ , although it does result in slightly better fits.

The marginal ( $2.1\sigma$  significant) increase of  $L_{disk}/L_X$  with  $L_{int}/L_{Edd}$  might also be caused by the onset of the RIAF. As  $R_t$  expands outwards, the disk emission decreases and the RIAF emission increases. The RIAF hot plasma emission is mostly X-ray bremsstrahlung and Compton up-scattering (like the corona), with an additional IR synchrotron component (which we discuss in Sections 4.3). As accretion rate drops and  $R_t$  increases, the rise of the RIAF X-ray emission compared to the optical/UV disk emission is seen as a decrease of  $L_{disk}/L_X$ . Indeed, local low-luminosity AGNs have even lower accretion rates and larger  $R_t$ , with consequently lower  $L_{disk}/L_X$  ratios and cooler optical thin-disk emission (Ho 2008).

The transition to an inner RIAF also causes the disappearance of broad emission lines at  $L_{int}/L_{Edd} \lesssim 0.01$ . Nicastro (2000) was the first to elegantly show that the broad emission lines are only present above

a critical accretion rate. However Nicastro (2000) assumed that the innermost possible orbit was given by the Shakura & Sunyaev (1973) thin-disk model,  $r_{crit} \simeq 8.16R_g$ . Here we follow their basic derivation, with the key difference that we use the RIAF transition radius as the innermost orbit for the presence of a broad-line region.

There is evidence that the broad emission line region is part of a disk wind (e.g. Emmering et al. 1992; Murray & Chiang 1998; Elvis 2000; Elitzur & Shlosman 2006). The positions of individual broad emission lines are stratified and set by the ionizing luminosity of the continuum (e.g. Peterson & Bentz 2006; Denney et al. 2009). The base of the wind itself, however, is set by the radius at which the radiation pressure equals the gas pressure, defined by Shakura & Sunyaev (1973) as:

$$\frac{r_{wind}}{(1 - r_{wind}^{-0.5})^{16/21}} \simeq 15.2(\alpha M)^{2/21} \left(\frac{\dot{m}}{\eta}\right)^{16/21}, \quad (8)$$

with  $r_{wind}$  in units of  $R/(6R_g) = R/(6GM/c^2)$ ,  $M$  in units of  $M_{BH}/M_\odot$ ,  $\alpha$  is the viscosity parameter, and  $\eta$  is the accretion efficiency. While RIAFs are expected to have strong outflows (see Section 4.2), the RIAF region is a high-temperature ionized plasma and so any associated disk wind would not emit broad emission lines in the UV/optical. Thus the RIAF truncation radius sets the innermost possible radius for the existence of a broad-line region. Assuming that  $\dot{m} \simeq L_{int}/L_{Edd}$  and rearranging Equation 8 with  $r_{wind} > R_t$ ,  $\alpha \simeq 0.1$ , and  $\eta \simeq 0.1$ , this sets the minimum specific accretion rate for a broad line region as:

$$\dot{m} \gtrsim 0.013(R_t/80R_g)M_8^{-1/8}, \quad (9)$$

with  $M_8 = M_{BH}/(10^8 M_\odot)$ . We leave  $R_t$  as a free parameter since it is poorly constrained, although the best-fit RIAF models for  $L_{int}/L_{Edd} \sim 10^{-3} - 10^{-2}$  AGNs suggest  $R_t \sim 80R_g$  (Yuan & Narayan 2004). As an AGN drops below this minimum accretion rate, its broad lines disappear and only narrow lines (or no lines) are observed, as seen in the transition at  $\log(L_{int}/L_{Edd}) \sim -2$  transition in Figures 5 and 6.

Elitzur & Ho (2009) also predict that the disk wind associated with the BLR will disappear below an accretion rate at which the outflowing velocity drops below the random velocity of the disk. Elitzur & Ho (2009) measure a BLR-disappearance accretion rate of  $\log(L/L_{Edd}) < C + \beta \log(L_{bol})$  from the low-luminosity local AGNs of Ho (2009), with  $\beta = -0.5$  and  $C = 14.4$ . In our sample (as well as those of Kollmeier et al. 2006; Trump et al. 2009b), the BLR disappears at  $\log(L/L_{Edd}) < 0.01$ . For a typical bolometric luminosity of  $L_{int} \sim 10^{44.5} \text{ erg s}^{-1}$  (also appropriate for the Kollmeier et al. 2006, sample), and assuming the same  $\beta = -0.5$ , this instead corresponds to  $C = 20.3$ : a remarkable difference of 6 orders of magnitude. It is unlikely that the bolometric corrections of Ho (2009) are incorrect by 6 orders of magnitude, and so we must conclude that the Elitzur & Ho (2009) model does not describe the disappearance of the BLR for high luminosity AGNs. Instead a disk-wind model following Nicastro (2000) best describes the BLR disappearance as the radius of wind generation region moves within the inner RIAF region.

It must be noted that while disk wind models have had success in describing highly ionized emission and absorption lines in the UV (Proga et al. 2000; Proga & Kallman 2004), they have not been applied to optical emission lines. The  $H\alpha$  broad emission line almost certainly forms in a higher density, lower ionization region than the C IV and Mg II broad emission lines. In addition there is evidence that the dynamics of the  $H\beta$  broad emission line are wildly variable, with reverberation mapping indicating infalling, virialized, and outflowing  $H\beta$  emission regions in three AGNs (Denney et al. 2009). While we do find that broad  $H\beta$  tends to be present only for  $L_{int}/L_{Edd} \gtrsim 0.01$  and so fits in the wind/RIAF framework, we do not study  $H\alpha$  and cannot say if this line is described by the same physics. Indeed, Ho (2009) present several AGNs with broad  $H\alpha$  emission and  $L_{int}/L_{Edd} < 10^{-3}$ . This suggests that broad  $H\alpha$  emission may have its origin outside the disk wind, although it is important to note that the accretion rates of Ho (2009) rely on bolometric corrections to monochromatic luminosities and so may suffer from significant systematic uncertainties.

#### 4.2. Accretion Rate and Outflows

The gas in a RIAF is not gravitationally bound to the supermassive black hole because the ions are not losing energy through radiation. As a result, AGNs with RIAFs are predicted to have strong radio outflows (Narayan et al. 1995; Meier 2001). The coupling between a RIAF and a strong radio outflow has been confirmed by observations of black hole binaries (Fender & Belloni 2004), and it is possible to translate these observations to AGN scales (e.g. Maccarone et al. 2003). In Figure 7 we show the AGNs of our sample with the ratio of radio luminosity to disk luminosity. Note that since the radio emission is coincident with the X-ray point source we assume that it originates from the AGN, but we cannot strictly rule out other sources of radio emission (e.g., from star formation). The  $L_{int}/L_{Edd} < 10^{-2}$  AGNs which are expected to have RIAFs tend to have higher ratios of radio to disk (optical/UV) luminosity. The mean  $L_{disk}/L_{radio}$  for rapidly accreting broad-line AGNs is a factor of ten lower than the mean  $L_{disk}/L_{radio}$  for narrow-line and lineless AGNs, and since the scatter in each sample is about  $\sim 0.5$  dex this translates to a highly significant difference ( $14.9\sigma$ ).

The large scatter in the  $L_{disk}/L_{radio}$  ratio at both high and low accretion rates is likely because the radio power is additionally dependent on properties like black hole spin and orientation. But the highly significant increase in  $L_{disk}/L_{radio}$  for low accretion rate AGNs suggests that  $L_{int}/L_{Edd} < 10^{-2}$  AGNs with RIAFs generally have relatively brighter radio emission. Melendez et al. (2010) noticed a similar trend of increasing radio luminosity with decreasing accretion rate, using [OIV] as a proxy for intrinsic luminosity (e.g., Melendez et al. 2008; Diamond-Stanic et al. 2009). Many nearby radio galaxies are also measured to have low accretion rates and may even have their optical/UV emission dominated by synchrotron emission rather than a thermal disk (Chiaberge et al. 1999).

In general, the radiation and disk winds of AGNs are thought to cause feedback on galaxy scales by quenching star formation (e.g., Hopkins et al. 2006;

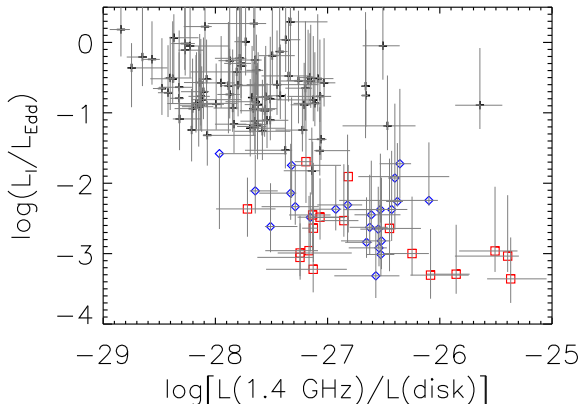


FIG. 7.— Accretion rate with a measure of radio brightness: the ratio of radio luminosity to disk luminosity for the 118 unobscured ( $N_H < 10^{22} \text{ cm}^{-2}$ ) AGNs in our sample. Broad-line AGNs are shown by black crosses, narrow-line AGNs by blue diamonds, and lineless AGNs by red squares. Narrow-line and lineless AGNs, at lower accretion rates than broad-line AGNs, tend to be more radio luminous compared to their accretion disk luminosity.

Hopkins & Elvis 2010), while radio jets are thought to cause larger-scale feedback which can heat the cores of galaxy clusters (e.g., Fabian et al. 2002) and is observed as extended emission line regions (Fu & Stockton 2009). The fact that RIAFs tend to have stronger radio emission suggests that weakly accreting AGNs may remain important for large-scale radio-mode feedback despite their optical/UV and X-ray luminosities. This suggests that heating cluster cores may not require bright quasars, but can be accomplished by faint AGNs (see also Hart et al. 2009). Allen et al. (2006) similarly found that several nearby weakly accreting AGNs had most of their Bondi accretion rates converted to radio outflows.

#### 4.3. Accretion Rate and the IR “Torus”

A clumpy dust “torus” emits a unique power-law signature in the mid-IR from  $\sim 1\text{--}10\mu\text{m}$  (Nenkova et al. 2008). This was first noticed observationally as a distinct AGN locus in Spitzer/IRAC color-color space (Lacy et al. 2004; Stern et al. 2005), although Donley et al. (2007) show that power-law selection is the most effective way to select AGN in the mid-IR. We compute the IR power-law slope in our AGNs from the host-subtracted observed IRAC photometry within the rest-frame wavelength range  $1 < \lambda < 10\mu\text{m}$ , shown with accretion rate in Figure 8. Type 1 AGNs typically have  $\alpha_{IR} < 0.5$  ( $\beta_{IR} < -0.5$  in terms of the  $f_\nu \sim \nu^\beta$  form used by Donley et al. 2007), matching the predictions of clumpy dust models (Nenkova et al. 2008). About 10% of Type 1 AGNs are “hot-dust-poor” and do not satisfy the  $\alpha_{IR}$  selection criterion<sup>14</sup>, about half of the narrow-line AGNs and only one of the lineless AGNs lack this torus signature. Cardamone et al. (2008) similarly found that many X-ray AGNs did not have a mid-IR power-law, although they did not track it with accretion rate. In our sample, the rapidly accreting broad-line AGNs have a mean  $\alpha_{IR} = 0.38 \pm 0.35$ , while the weakly accreting narrow-line and lineless AGNs have a mean  $\alpha_{IR} = 1.26 \pm 0.72$ ,

<sup>14</sup> For more details on this population, see Hao et al. (2010).

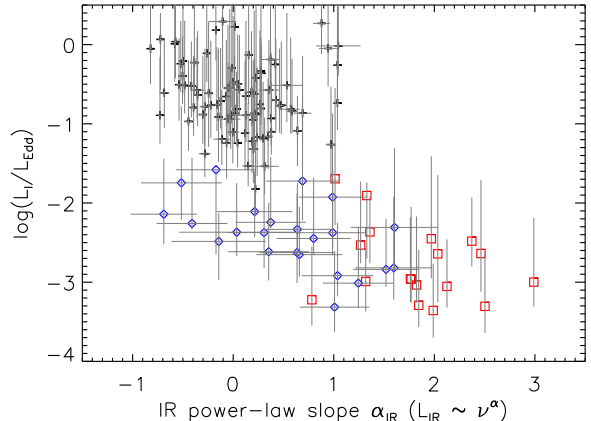


FIG. 8.— Accretion rate with the power-law slope of the  $1 < \lambda < 10\mu\text{m}$  IR emission for the 118 unobscured ( $N_H < 10^{22} \text{ cm}^{-2}$ ) AGNs. As in previous figures, black crosses are broad-line AGNs, blue diamonds are narrow-line AGNs, and red squares are lineless AGNs. We measure the slope  $\alpha_{IR}$  as  $L \sim \nu^\alpha$ , corresponding to the slope  $\beta$  used in the power-law selection of Donley et al. (2007) as  $\beta = \alpha_{IR} - 1$ . Most high accretion rate ( $L_{int}/L_{Edd} > 0.01$ ) AGNs have IR power-law slopes corresponding to a dusty torus ( $\alpha_{IR} < 0.5$ ). Of  $L_{int}/L_{Edd} < 0.01$  AGNs, however, half the narrow-line and all but one of the lineless AGNs lack the torus signature.

meaning that the two samples differ with high significance ( $10.7\sigma$ ).

A unified model based solely on geometrical obscuration suggests that narrow-line and lineless AGNs are obscured by the same torus present in broad-line AGNs (e.g., Antonucci 1993). Instead the low accretion rate AGNs ( $L_{int}/L_{Edd} < 0.01$ ) frequently lack the torus IR signature. In part, this may be because the torus power-law is simply being overwhelmed by the accretion disk SED at  $L_{int}/L_{Edd} < 0.01$ . At low accretion rates, the temperature of the disk decreases, and a disk with  $E_{peak} = 1 \text{ eV}$  will peak at  $1.2 \mu\text{m}$ , emitting a power-law of  $\alpha \sim 2$  at  $1 < \lambda < 10\mu\text{m}$ . In a typical broad-line AGN, the IR torus is roughly the same strength as the accretion disk (Richards et al. 2006, see also Figure 2). Since many  $L_{int}/L_{Edd} < 0.01$  AGNs in Figure 8 have  $\alpha \gtrsim 2$ , they must be dominated by the accretion disk emission and have, at best, very little emission from the torus.

The weaker or missing torus in many  $L_{int}/L_{Edd} < 0.01$  AGNs can be described in a similar fashion to the vanishing disk-wind BLR in Section 4.1. There is good evidence that the outer edge of the BLR coincides with the inner edge of the clumpy dust (Netzer & Laor 1993; Suganuma et al. 2006). Some authors additionally suggest that the BLR and the clumpy dust “torus” are two components of the same wind driven off the accretion disk (e.g., Elitzur & Shlosman 2006). If the clumpy dust wind emerges from the disk at a similar radius to that calculated in Section 4.1, then we would expect the IR power-law signature to disappear at  $L_{int}/L_{Edd} < 0.01$ , just as the BLR disappears. However many narrow-line AGNs with  $L_{int}/L_{Edd} < 0.01$  still have the negative IR power-law slopes, suggesting that there must be another source of mid-IR emission. Either there is a distant source of clumpy dust beyond the expanding RIAF, or there is mid-IR synchrotron emission in the RIAF region at the base of the radio jet (as observed by Leipski et al. 2009).

## 5. A SIMPLE MODEL FOR UNIFYING AGNS BY SPECIFIC ACCRETION RATE

Figure 9 presents a simple schematic outlining the changes in AGNs from high ( $L_{int}/L_{Edd} > 0.01$ ) to low ( $L_{int}/L_{Edd} < 0.01$ ) accretion rate. At the top is a broad-line AGN with high accretion rate ( $L_{int}/L_{Edd} \sim 0.1$ ). At these high accretion rates the gas and dust falling into the black hole forms a thin accretion disk and a disk wind originates at  $R_{wind} \sim 250R_g$ . The broad emission lines are emitted in stratified regions along this wind based on the radiation pressure (which ionizes and excites the wind material), with  $R_{BLR} \sim L^{0.5}$  and high ionization lines (e.g., C IV) emitted from nearer radii than low ionization lines (e.g., Mg II) (Peterson & Bentz 2006). At higher radii, the disk wind forms clumpy dust (Nenkova et al. 2008). This dusty “torus” can obscure the AGN along lines of sight near the disk, causing an observer to see an obscured narrow-line AGN (Antonucci 1993).

The bottom of Figure 9 shows an AGN with low accretion rate ( $L_{int}/L_{Edd} \sim 0.003$ ), characteristic of the unobscured narrow-line and lineless AGNs in our sample. The onset of a geometrically thick RIAF changes the picture dramatically. Because the disk wind radius is within the RIAF, there are no broad emission lines. Instead the dominant outflow is a radio jet, and AGNs with low accretion rates and RIAFs are typically more radio luminous than broad-line AGNs. The lack of a disk wind also means that there is not the typical clumpy dust “torus” seen in broad-line AGNs. However we cannot rule out the presence of dust completely, as clumpy dust may come from another source besides the disk wind and some  $L_{int}/L_{Edd} \lesssim 0.01$  have the IR signature of hot dust.

## 6. PREDICTIONS AND FUTURE OBSERVATIONAL TESTS

The multiwavelength data of COSMOS provide many diagnostic capabilities, and we have argued that decreasing accretion rates lead to the onset of a RIAF at  $\dot{m} < 0.01$  and subsequently stronger radio jets, a weaker torus, and the disappearance of broad emission lines. The onset of a RIAF also makes several predictions testable by future observations. In addition the simple model in Section 5 can be more fully constrained by additional investigations.

If the broad-line region is truly disappearing at  $\dot{m} < 0.01$  then we would expect spectropolarimetry to reveal reflected broad emission lines in only high accretion rate ( $\dot{m} > 0.01$ ) narrow-line and lineless AGNs.

Spectropolarimetry of nearby AGNs shows a dichotomy based on accretion rate, although most authors place the change from hidden broad lines to “true” Type 2 AGN at  $\dot{m} \sim 0.001$  (Tran 2003; Wang & Zhang 2007). Most likely, the difference results from the uncertain bolometric corrections used in these previous works, compared to the full modeled SEDs used here.

Mid-IR broad-band polarimetry could determine the cause of the negative IR power-law slopes in  $\dot{m} < 0.01$  AGNs. If the clumpy dust “torus” is associated with the same wind that drives the broad line region, it should disappear in these objects. The mid-IR signature might instead be synchrotron radiation in the RIAF at the base of the jet, which would appear polarized at the  $> 3\%$  level (e.g., Jannuzi et al. 1994). If no polarization is detected, then we must conclude that clumpy dust exists at higher radii than the BLR disk-wind, beyond the RIAF region of  $\dot{m} < 0.01$  AGNs.

It is very difficult to measure accretion rates of partially or fully obscured AGNs, and such objects are generally missed by the X-ray and optical limits of this study. However we do make a few predictions for the accretion rates of various AGNs. If the torus is part of a disk-wind that vanishes at  $\dot{m} < 0.01$ , then torus-obscured AGNs of the classical Antonucci (1993) unified model will have only high accretion rates ( $\dot{m} > 0.01$ ). Obscuration by cooler dust associated with host galaxy star formation, as predicted by the observed redshift evolution in the narrow-line/broad-line AGN ratio (Treister et al. 2009; Trump et al. 2009a), could conceivably be present at any accretion rate (although it may be limited by the ability of the dusty star formation to feed the black hole, Ballantyne 2008). We might then expect that obscured AGNs with a strong mid-IR torus signature should have  $\dot{m} > 0.01$ , while AGNs obscured by the cooler dust associated with host galaxy star formation might have a wider range of accretion rates.

JRT acknowledges support from NSF/DDEP grant #0943995, and with CDI acknowledges support from NSF grant #AST-0908044. BCK acknowledges support from NASA through Hubble Fellowship grant #HF-51243.01 awarded by the Space Telescope Science Institute, which is operated by the Association of Universities for Research in Astronomy, Inc., for NASA, under contract NAS 5-26555.

## REFERENCES

- Allen, S. W., Dunn, R. J. H., Fabian, A. C., Taylor, G. B. & Reynolds, C. S. 2006, MNRAS, 372, 21  
 Antonucci, R. 1993, ARA&A, 31, 473  
 Arnouts, S. et al. 2007, A&A, 476, 137  
 Baldwin, J. A., Phillips, M. M., & Terlevich, R. 1981, PASP, 93  
 Ballantyne, D. R. 2008, ApJ, 685, 787  
 Barth, A. J., Filippenko, A. V. & Moran, E. C. 1999, ApJ, 525, 673  
 Begelman, M. C., Blandford, R. D. & Rees, M. J. 1984, RvMP, 56, 255  
 Bentz, M. C., Peterson, B. M., Pogge, R. W., Vestergaard, M., & Onken, 2006, C. A. ApJ, 644, 133  
 Bianchi, S. et al. 2008, MNRAS, 385, 195  
 Bongiorno, A. et al. 2007, A&A, 472, 443  
 Brandt, W. N., & Hasinger, G. 2005, ARA&A, 43, 827  
 Brusa, M. et al. 2010, ApJ, 716, 348  
 Caccianiga, A., Severgnini, P., Della Ceca, R., Maccacaro, T., Carrera, F. J., & Page, M. J., A&A, 470, 557  
 Capak, P. et al. 2010, in prep.  
 Cappelluti, N. et al. 2009, A&A, 497, 635  
 Cardamone, C. N. et al. 2008, ApJ, 680, 130  
 Cash, W. 1979, ApJ 228, 939  
 Chiaberge, M., Capetti, A. & Celotti, A. 1999, A&A, 349, 77  
 Comastri, A. et al. 2002, ApJ, 571, 771  
 Davies, R. I. et al. 2006, ApJ, 646, 754  
 Decarli, R. et al. 2010, MNRAS, 402, 2453  
 Denney, K. D. et al. 2009, ApJ, 704, 80  
 Di Matteo, T., Springel, V., & Hernquist, L. 2005, Nature, 433, 604

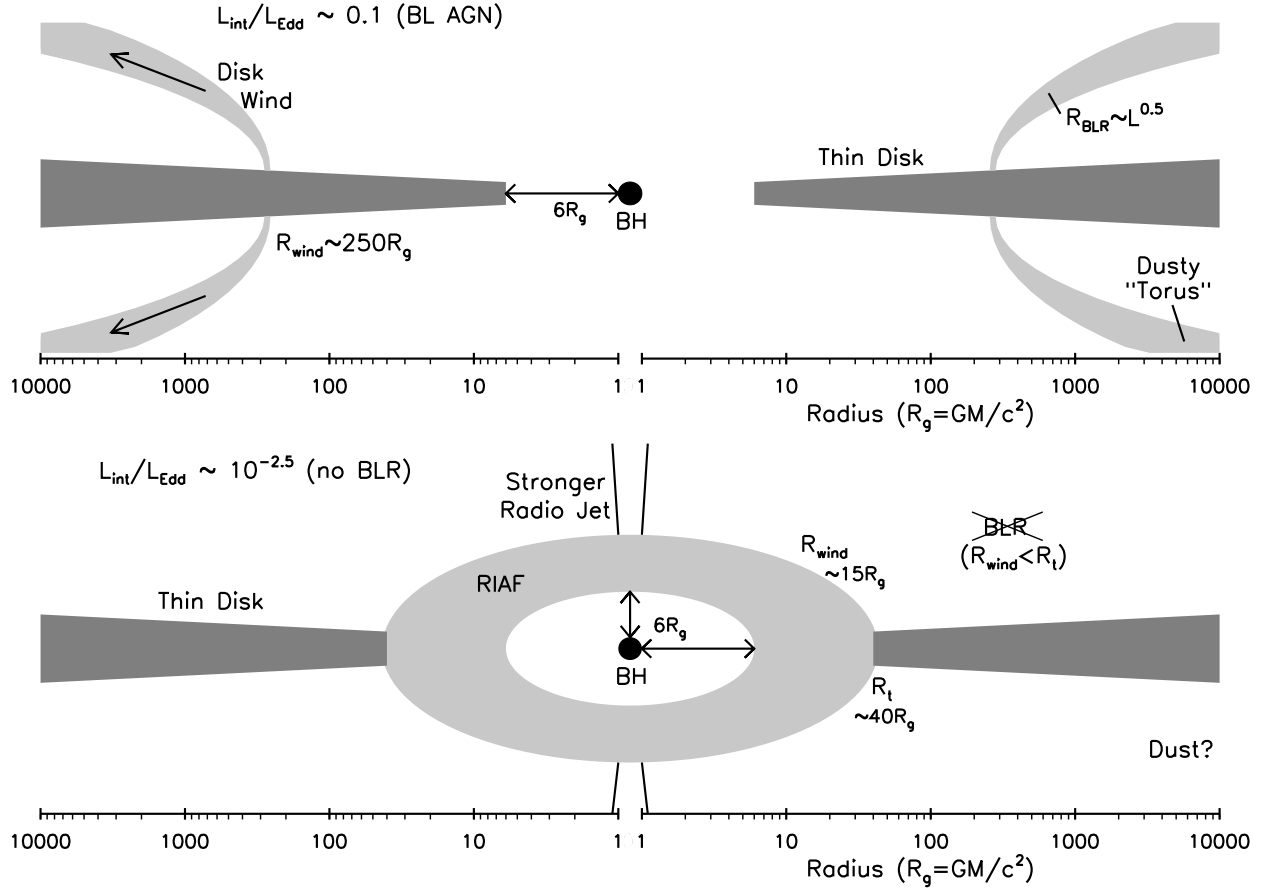


FIG. 9.— A schematic model showing the changes in the accretion disk from a broad-line AGN with high accretion rate ( $L_{int}/L_{Edd} \sim 0.1$ ) to a narrow-line or lineless AGN with low accretion rate ( $L_{int}/L_{Edd} \sim 0.003$ ). The x axis shows the radial distance from the black hole in units of  $GM/c^2$ . The y axis is qualitative only. At  $L_{int}/L_{Edd} \lesssim 0.01$ , the disk wind falls inside the RIAF. As a result there are no broad emission lines, the hot dust signature becomes very different, and the radio jet becomes stronger.

- Diamond-Stanic, A. M., Rieke, G. H. & Rigby, J. R. 2009, *ApJ*, 698, 623  
 Dietrich, M. & Hamann, F. 2004, *ApJ*, 611, 761  
 Donley, J. L., Rieke, G. H., Perez-Gonzalez, P. G., Rigby, J. R., & Alonso-Herrero, A. 2007, *ApJ*, 660, 167  
 Elitzur, M. & Shlosman, I. 2006, *ApJ*, 648, L101  
 Elitzur, M. & Ho, L. C. 2009, *ApJ*, 701, L91  
 Elvis, M., Schreier, E. J., Tonry, J., Davis, M., & Huchra, J. P. *ApJ*, 246, 20  
 Elvis, M. 2000, *ApJ*, 545, 63  
 Elvis, M. et al. 2009, *ApJS*, 184, 158  
 Emmering, R. T., Blandford, R. D. & Shlosman, I. 1992, *ApJ*, 385, 460  
 Eracleous, M., Hwang, J. A. & Flohic, H. M. 2010, *ApJ*, 711, 796  
 Fabian, A. C., Celotti, A., Blundell, K. M., Kassim, N. E., & Perley, R. A. 2002, *MNRAS*, 331, 369  
 Fender, R. & Belloni, T. 2004, *ARA&A*, 42, 317  
 Ferrarese, L. & Merritt, D. 2000, *ApJ*, 593, 9  
 Fu, H. & Stockton, A. 2009, *ApJ*, 690, 953  
 Gabor, J. M. et al. 2009, *ApJ*, 691, 705  
 Gebhardt, K. et al. 2000, *ApJ*, 539, 13  
 Gierliński, M., Zdziarski, A. A., Poutanen, J., Coppi, P. S., Ebisawa, K. & Johnson, W. N. 1999, *MNRAS*, 309, 496  
 Gilli, R., Comastri, A., & Hasinger, G. 2007, *A&A*, 463, 79  
 Gliozzi, M., Sambruna, R. M., & Foschini, L. 2007, *ApJ*, 662, 878  
 Graham, A. W. 2007, *MNRAS*, 379, 711  
 Greene, J. E., & Ho, L. C. 2006, *ApJ*, 641, 21  
 Hao, H. et al. 2010, *ApJL* in press (arXiv:1009.3276)  
 Häring, N. & Rix, H.-W. 2004, *ApJ*, 604, L89  
 Hart, Q. N., Stocke, J. T., & Hallman, E. J. 2009, *ApJ*, 705, 854  
 Hawkins, M. R. S. 2004, *A&A*, 424, 519  
 Heckman, T. M. 1980, *A&A*, 87, 152  
 Ho, L. C. 2008, *ARA&A*, 46, 475  
 Ho, L. C. 2009, *ApJ*, 699, 626  
 Hopkins, P. F., Hernquist, L., Cox, T. J., di Matteo, T., Robertson, B., & Springel, V. 2006, *ApJS*, 163, 1  
 Hopkins, P. F., Richards, G. T., Hernquist, L. 2007, *ApJ*, 654, 731  
 Hopkins, P. F., Hickox, R., Quataert, E., & Hernquist, L. 2009, *MNRAS*, 398, 333  
 Hopkins, P. F. & Elvis, M. 2010, *MNRAS*, 401, 7  
 Hornschemeier, A. F. et al. 2001, *ApJ*, 554, 742  
 Ilbert, O. et al. 2009, *ApJ*, 690, 1236  
 Ilbert, O. et al. 2010, *ApJ*, 709, 644  
 Jahnke, K. et al. 2009, *ApJ*, 706, 215  
 Jannuzi, B. T., Smith, P. S. & Elston, R. 1994, *ApJ*, 428, 130  
 Kaspi, S., Brandt, W. N., Maoz, D., Netzer, H., Schneider, D. P. & Shemmer, O. 2007, *ApJ*, 659, 997  
 Kelly, B. C., Bechtold, J., Trump, J. R., Vestergaard, M., & Siemiginowska, A. 2008, *ApJS*, 176, 3557  
 Kelly, B. C., Vestergaard, M., Fan, X., Hopkins, P. F., Hernquist, L. & Siemiginowska, A. 2010, *ApJ* in press (astro-ph/1006.3561)  
 Koekemoer, A. M. et al. 2007, *ApJS*, 172, 196  
 Kollmeier, J. A. et al. 2006, *ApJ*, 648, 128  
 Krolik, J. H., & Begelman, M. C. 1988, *ApJ*, 329, 702  
 Lacy, M. et al. 2004, *ApJS*, 154, 166  
 Laor, A. 2003, *ApJ*, 590, 86  
 Lauer, T. R., Tremaine, S., Richstone, D., & Faber, S. M. 2007, *ApJ*, 670, 249  
 Leipski, C., Antonucci, R., Ogle, P. & Whysong, D. 2009, *ApJ*, 701, 891  
 Lilly, S. J. et al. 2007, *ApJS*, 172, 70  
 Maccarone, T. J., Gallo, E. & Fender, R. 2003, *MNRAS*, 345, L19  
 Magorrian, J. et al. 1998, *AJ*, 115, 2285

- Mainieri, V. et al. 2007, ApJS, 172, 368  
Maiolino, R., Marconi, A., & Oliva, E. 2001, A&A, 365, 37  
Marconi, A. & Hunt, L. K. 2003, ApJ, 589, 21  
Marconi, A., Risaliti, G., Gilli, R., Hunt, L. K., Maiolino, R. & Salvati, M. 2004, MNRAS, 351, 169  
Marconi, A. et al. 2008, ApJ, 678, 693  
Martinez-Sansigre, A. et al. 2006, MNRAS, 370, 1479  
McCracken, H. J. et al. 2010, ApJ, 708, 202  
Meier, D. L. 2001, ApJ, 548, L9  
Melendez, M. et al. 2008, ApJ, 682, 94  
Melendez, M., Kraemer, S. B. & Schmitt, H. R. 2010, MNRAS in press (astro-ph/1003.2984)  
Merloni, A. et al. 2010, ApJ, 708, 137  
Molina, M. et al. 2006, MNRAS, 371, 821  
Mor, R., Netzer, H., & Elizur, H. 2009, ApJ, 705, 298  
Moran, E. C., Filippenko, A. V., & Chornock, R. 2002, ApJL, 579, 71  
Murray, N. & Chiang, J. 1998, ApJ, 494, 125  
Narayan, R., Yi, I. & Mahadevan, R. 1995, Nature, 374, 623  
Narayan, R. & McClintock, J. E. 2008, NewAr, 51, 733  
Nenkova, M., Sirocky, M. M., Nikutta, R., Ivezić, Ž. & Elitzur, M. et al. 2008, ApJ, 685, 160  
Netzer, H. & Laor, A. 1993, ApJ, 404, 51  
Nicastro, F. 2000, ApJ, 530, L65  
Nicastro, F., Martocchia, A. & Matt, G. 2003, ApJ, 589, L13  
Onken, C. A., Ferrarese, L., Merritt, D., Peterson, B. M., Pogge, R. W., Vestergaard, M., & Wandel, A. 2004, ApJ, 615, 645  
Onken, C. A. et al. 2007, ApJ, 670, 105  
Pacynski, B. & Wiita, P. K. 1980, A&A, 88, 23  
Pei, Y. C. 1992, ApJ, 395, 130  
Perola, G. C. et al. 2002, 389, 802  
Peterson, B. M. & Bentz, M. C. 2006, NewAR, 50, 796  
Polletta, M. et al. 2007, ApJ, 663, 81, 102  
Proga, D., Stone, J. M., & Kallman, T. R. 2000, ApJ, 543, 686  
Proga, D. & Kallman, T. R. 2004, ApJ, 616, 688  
Ptak, A., Terashima, Y., Ho, L. C. & Quataert, E. 2004, ApJ, 606, 173  
Richards, G. T. et al. 2003, AJ, 126, 1131  
Richards, G. T. et al. 2006, ApJ, 166, 470  
Schinnerer, E. et al. 2007, ApJS, 172, 46S  
Scoville, N. et al. 2007, ApJS, 172, 38  
Shakura, N. I., & Sunyaev, R. A. 1973, A&A, 24, 337  
Shen, Y., Greene, J. E., Strauss, M. A., Richards, G. T., & Schneider, D. P. 2008, ApJ, 680, 169  
Shen, Y. & Kelly, B. C. 2010, ApJ, 713, 41  
Shi, Y. et al. 2009, ApJ, 703, 1107  
Silverman, J. D. et al. 2009, ApJ, 696, 396  
Simon, L. E. & Hamann, F. 2010, MNRAS, 407, 1826  
Soltan, A. 1982, MNRAS, 200, 115  
Stern, D. et al. 2005, ApJ, 631, 163  
Suganuma, M. et al. 2006, ApJ, 639, 46  
Tananbaum, H. et al. 1979, ApJ, 234, L9  
Tran, H. D. 2001, ApJ, 554, L19  
Tran, H. D. 2003, ApJ, 583, 632  
Treister, E. et al. 2004, ApJ, 616, 123  
Treister, E. et al. 2009, ApJ, 693, 1713  
Trouille, L., Barger, A. J., Cowie, L. L., Yang, Y., & Mushotzky, R. F. 2009, ApJ, 703, 2160  
Trump, J. R. et al. 2007, ApJS, 172, 383  
Trump, J. R. et al. 2009a, ApJ, 696, 1195  
Trump, J. R. et al. 2009b, ApJ, 700, 49  
Trump, J. R. et al. 2009c, ApJ, 706, 797  
Ueda, Y. et al. 2003, ApJ, 598, 886  
Urry, C. M. & Padovani, P. 1995, PASP, 107, 803  
Vanden Berk, D. E. et al. 2001, AJ, 122, 549  
Vasudevan, R. V. & Fabian, A. C. 2009, MNRAS, 392, 1124  
Vestergaard, M. 2004, ApJ, 601, 676  
Vestergaard, M. & Peterson, B. M. 2006, ApJ, 641, 689  
Vestergaard, M. & Osmer, P. S. 2009, 699, 800  
Vignali, C., Brandt, W. N., Schneider, D. P., Garmire, G. P., & Kaspi, S. 2003, AJ, 125, 2876  
Wang, J.-M. & Zhang, E.-P. 2007, ApJ, 660, 1072  
Young, M., Elvis, M. & Risaliti, G. 2010, ApJ, ApJ, 708, 1388  
Younger, J. D. et al. 2008, ApJ, 686, 815  
Yuan, F. & Narayan, R. 2004, ApJ, 612, 724  
Yuan, F. 2007, in ASP Conf. Ser. 373, The Central Engine of Active Galactic Nuclei, ed. L. C. Ho & J.-W. Wang (San Francisco, CA: ASP), 95  
Zamojski, M. A. 2007, ApJS, 172, 468

TABLE 2  
CATALOG OF AGNs<sup>a</sup>

RA+Dec (J2000) hhmmss.ss+ddmmss.s	Type <sup>b</sup>	Redshift	Spec. <sup>c</sup> source	$L_{int}$ $\log(L_{\odot})$	$M_{BH}$ $\log(M_{\odot})$	$\log(L_{int}/L_{Edd})$
095728.34+022542.2	BL	1.54	S	46.03 <sup>+0.52</sup> <sub>-0.10</sub>	8.40 <sup>+0.36</sup> <sub>-0.43</sub>	-0.49 <sup>+0.58</sup> <sub>-0.27</sub>
095740.78+020207.9	BL	1.48	I	45.88 <sup>+0.64</sup> <sub>-0.30</sub>	8.24 <sup>+0.45</sup> <sub>-0.39</sub>	-0.47 <sup>+0.68</sup> <sub>-0.40</sub>
095743.33+024823.8	BL	1.36	S	45.84 <sup>+0.66</sup> <sub>-0.16</sub>	8.24 <sup>+0.44</sup> <sub>-0.36</sub>	-0.51 <sup>+0.18</sup> <sub>-0.66</sub>
095749.02+015310.1	NL	0.32	I	43.89 <sup>+0.71</sup> <sub>-0.21</sub>	8.61 <sup>+0.29</sup> <sub>-0.30</sub>	-2.84 <sup>+0.73</sup> <sub>-0.15</sub>
095750.20+022548.3	BL	1.24	Z	44.93 <sup>+0.52</sup> <sub>-0.20</sub>	7.28 <sup>+0.38</sup> <sub>-0.41</sub>	-0.46 <sup>+0.60</sup> <sub>-0.28</sub>
095752.17+015120.1	BL	4.16	Z	46.28 <sup>+0.69</sup> <sub>-0.10</sub>	8.71 <sup>+0.41</sup> <sub>-0.42</sub>	-0.54 <sup>+0.53</sup> <sub>-0.36</sub>
095752.17+015120.1	BL	4.17	I	46.26 <sup>+0.54</sup> <sub>-0.07</sub>	8.66 <sup>+0.38</sup> <sub>-0.44</sub>	-0.51 <sup>+0.52</sup> <sub>-0.31</sub>
095753.49+024736.1	BL	3.61	I	46.24 <sup>+0.75</sup> <sub>-0.27</sub>	8.00 <sup>+0.49</sup> <sub>-0.40</sub>	0.12 <sup>+0.69</sup> <sub>-0.46</sub>
095754.11+025508.4	BL	1.57	S	46.21 <sup>+0.66</sup> <sub>-0.49</sub>	8.70 <sup>+0.39</sup> <sub>-0.41</sub>	-0.61 <sup>+0.65</sup> <sub>-0.32</sub>
095754.70+023832.9	BL	1.60	S	46.14 <sup>+0.54</sup> <sub>-0.24</sub>	8.72 <sup>+0.40</sup> <sub>-0.41</sub>	-0.69 <sup>+0.47</sup> <sub>-0.39</sub>
095755.08+024806.6	BL	1.11	S	45.94 <sup>+0.62</sup> <sub>-0.17</sub>	8.43 <sup>+0.36</sup> <sub>-0.43</sub>	-0.60 <sup>+0.57</sup> <sub>-0.28</sub>
095755.34+022510.9	BL	2.74	I	45.51 <sup>+0.45</sup> <sub>-0.07</sub>	8.07 <sup>+0.36</sup> <sub>-0.45</sub>	-0.68 <sup>+0.44</sup> <sub>-0.36</sub>
095755.48+022401.1	BL	3.10	I	46.82 <sup>+0.78</sup> <sub>-0.47</sub>	8.44 <sup>+0.42</sup> <sub>-0.45</sub>	0.27 <sup>+0.79</sup> <sub>-0.24</sub>
095759.50+020436.1	BL	2.03	S	46.82 <sup>+0.70</sup> <sub>-0.46</sub>	8.94 <sup>+0.38</sup> <sub>-0.40</sub>	-0.23 <sup>+0.32</sup> <sub>-0.56</sub>
095759.91+021634.5	BL	1.54	I	44.68 <sup>+0.67</sup> <sub>-0.10</sub>	8.26 <sup>+0.45</sup> <sub>-0.39</sub>	-1.70 <sup>+0.46</sup> <sub>-0.37</sub>
095801.61+020428.9	BL	1.23	Z	45.43 <sup>+0.76</sup> <sub>-0.26</sub>	8.28 <sup>+0.33</sup> <sub>-0.39</sub>	-0.96 <sup>+0.76</sup> <sub>-0.26</sub>
095802.10+021541.0	OD	0.94	I	45.05 <sup>+0.59</sup> <sub>-0.06</sub>	9.44 <sup>+0.38</sup> <sub>-0.33</sub>	-2.50 <sup>+0.47</sup> <sub>-0.33</sub>
095805.10+020445.8	NL	0.67	I	44.91 <sup>+0.55</sup> <sub>-0.08</sub>	9.33 <sup>+0.34</sup> <sub>-0.39</sub>	-2.54 <sup>+0.72</sup> <sub>-0.20</sub>
095806.24+020113.8	NL	0.62	I	44.25 <sup>+0.65</sup> <sub>-0.28</sub>	9.03 <sup>+0.35</sup> <sub>-0.33</sub>	-2.90 <sup>+0.70</sup> <sub>-0.34</sub>
095806.99+022248.5	BL	3.10	I	46.39 <sup>+0.69</sup> <sub>-0.25</sub>	9.34 <sup>+0.36</sup> <sub>-0.43</sub>	-1.06 <sup>+0.68</sup> <sub>-0.31</sub>
095809.45+020532.4	OD	0.61	I	44.00 <sup>+0.48</sup> <sub>-0.33</sub>	9.26 <sup>+0.43</sup> <sub>-0.29</sub>	-3.38 <sup>+0.52</sup> <sub>-0.43</sub>

<sup>a</sup> The full catalog will appear as a machine-readable table in the electronic version.

<sup>b</sup> “BL” refers to a broad-line AGN, “NL” is a narrow-line AGN, and “OD” is a lineless or optically dull AGN.

<sup>c</sup> “S” means the spectrum and redshift are from the SDSS archive, “I” is from the COSMOS Magellan/IMACS campaign (Trump et al. 2009a), and “Z” is from the zCOSMOS VLT/VIMOS campaign (Lilly et al. 2007).